SLAC–PUB–4851
April 1989
(T/E)

THE STANFORD LINEAR COLLIDER – FALL 1988*

D. L. BURKE
*Stanford Linear Accelerator Center,
Stanford University, Stanford, California 94309*

ABSTRACT

This paper contains a description of the Stanford Linear Collider and a summary of its performance during recent periods of operation.

1. INTRODUCTION

The newest generation of high-energy e^+e^- colliding beam machines—SLC and LEP—will provide spectacular views of the weak interactions of quarks and leptons, and perhaps glimpses of what lies beyond the Standard Model. These machines will access center-of-mass energies between 80 and 200 GeV and will allow particle physicists to begin detailed studies of the Z° and $W^\pm$ gauge bosons responsible for the weak interactions. While the particle physics objectives of the two projects have much in common, the machines themselves are markedly different. The SLC is the first example of a linear e^+e^- collider. The development of the technology and accelerator physics associated with this type of machine is crucial if electron-positron annihilation is to remain a feasable means to explore particle physics at still higher mass scales.

The SLC has functioned reasonably well in its role as a project in linear collider research and development but has not yet proven to be a research tool for particle physics. The accelerator physics of this machine has been found, so far, to be essentially as expected, although operation at beam intensities above 2.5×10^{10} particles per pulse has yet to be fully confronted. Initial attempts this past Summer to do physics with this machine met with failure caused by extremely poor reliability of a number of hardware components of the machine and by cumbersome procedures needed to set up the beams for physics. Sixty hours of colliding

---

* Work supported by the Department of Energy, contract DE–AC03–76SF00515.

Invited talk presented at the Meeting of the Division of Particles and Fields of the APS, Storrs, Connecticut, August 15–18, 1988.

beams have been delivered for particle physics research and the Mark II experiment has logged thirty of these hours. Muons and electromagnetic debris created by stray beam particles that strike machine apertures were sufficiently intense to make it impossible to take usable data approximately 50% of the time. The luminosity of the accumulated exposure is estimated to be sufficient to have produced approximately 0.5 Z°s. No candidate annihilation events have been found in the Mark II data sample, but one two-photon event of the type $ee \rightarrow eeee$ has been uncovered.

2. PARTICLE PHYSICS AT THE Z°

The physics issues addressed by studies of electron-positron annihilation at center-of-mass energies near the mass of the Z°,

$$e^{+}e^{-} \rightarrow Z^{\circ}, \qquad \sqrt{s} \approx 93 \text{ GeV/c}^{2} \quad , \tag{1}$$

have been explored and documented in detail in a number of places[1] but it is useful to briefly review several benchmark cases to define goals for machine design and operation.

2.1 Precision Tests of the Standard Model

There are three parameters that must be determined before predictions can be made with the minimal Weinberg–Salam model of electroweak interactions (with $\rho \equiv 1$). Two of these parameters can be taken to be the electromagnetic fine-structure constant α_F and the muon decay constant G_{μ} both of which are known extremely well. A suitable third parameter is the mass of the Z°. Once this is measured then the dependence of the Z° production cross section on the spin direction (helicity) of the initial $e^{\pm}$, forward/backward asymmetries in the angular distributions of Z° decays to fermion pairs and low energy neutrino scattering cross sections will constitute rigorous tests of the theory.[2] If the theory is correct, these phenomena are characterised by a common electroweak interaction with universal strength.

With as few as 100 events it will be possible to determine $m_{Z^{\circ}}$ well enough ($\delta_m <$ 300 MeV) to calculate low-energy neutrino cross sections far more accurately than they can be measured. Precise tests of the theory will require the accumulation of 10^{6}–10^{7} Z°'s to reduce the statistical errors of the measurement of fermion production asymmetries to systematic levels. If the beams can be polarized, then with fewer Z°'s it will be possible to measure the spin dependence of the Z° cross section well enough to tighten the constraints on the theory even further. Data samples of 10^{5} Z°'s will suffice if even one of the beams can be polarized (50% polarization).

2.2 QCD

Three quarters of the total width of the Z° is expected to be generated by decays into quarks and gluons. Studies of gluon bremsstrahlung in events with three-and four-parton jets and comparisons with similar studies made at lower center-of-mass energies will yield important measurements of the Q^2 dependence of the strong coupling constant. In addition, well-chosen 4-jet events may result in observation of the self-coupling of the gluon field directly at the tree level. These quintessential signatures of the non–Abelian nature of QCD should be observable with data samples of 10^4–10^5 Z°s. As a point of reference, it should be noted that this is also the typical number of hadronic events acquired by experiments at PEP and PETRA.

2.3 The Generation Question

One of the most fundamental quantities that can be determined at the SLC and LEP is the width of the Z° due to its coupling to light, weakly-interacting electrically-neutral particles. The only such particles that we know of are neutrinos: ν_e, ν_μ, and ν_τ. Any deviation of the measured "invisible" width of the Z° from that expected from three generations of neutrinos would signal the existence of previously undiscovered particles. It is important to note that experimental searches that have been reported do not exclude the existence of such particles unless their coupling to the Z° is 2–3 times that of a neutrino generation.

Measurements of $\Gamma_{Z^\circ \to weakly\ interacting\ particles}$ can be made in several ways. The most promising for initial studies is to determine

$$\Gamma_{invisible} \equiv \Gamma_{total} - \Gamma_{visible} \tag{2}$$

by direct subtraction. A few thousand Z°s will be sufficient to determine $\Gamma_{invisible}$ with an accuracy that corresponds to one-third to one-half the partial width expected from a single neutrino species. With luminosities of 10^{30} or better it will be feasable to conduct experiments at $\sqrt{s}$ just above m_{Z° to radiativly produce Z°s,

$$e^+e^- \to \gamma Z^\circ \quad . \tag{3}$$

Events in which the Z° decays to only weakly interacting particles can be tagged by detecting the photon. This technique can be used to search for particles with coupling strengths to the Z° that are perhaps as small as 0.05–0.1 that of a neutrino species. The discovery reach of such a measurement would be extremely large.

2.4 Other New Particle Searches

The list of new particles that might appear in decays of the Z° is long—Higgs particles, SUSY particles, new heavy quarks and leptons.... A generic point of view can be taken by noting that present limits on the total width of the Z° still allow 20% or so of all Z°s to decay to previously unknown particles. Even a few hundred Z° events might reveal something new if its signature is sufficiently striking! More typically 10^4–10^6 events are needed to find and establish the properties of most of the particles people have imagined.

2.5 Summary of Particle Physics Goals

From the above brief discussions it seems that a reasonable initial goal for an experiment at the SLC will be to accumulate several thousand Z°s. Polarization is not a necessity, but the beam energy-spread should be sufficiently small and the energy profile well enough known to allow a determination of the mass of the Z° with a precision of $\delta_m \sim 100$ MeV. Complete exploration of the physics will require accumulation of several million Z°s, and it is highly desirable that at least one of the beams be polarized.

3. CHARACTERISTICS OF HIGH-ENERGY e^+e^- MACHINE

The energy profile of the beams, the luminosity generated by the collisions of the beams and perhaps the degree of beam polarization are the most basic quantities that determine the physics reach of a particular colliding beam machine. The locations of optical elements and the transverse and longitudinal sizes of the beams at the collision point and in the final lens system of the machine may severely constrain the design of experimental detectors. The duty cycle of the accelerator and backgrounds induced in the detectors by the beam are also factors that can diminish the usefulness of a particular machine.

At future high-energy machines the beam sizes and bunch intensities necessary to produce reasonable luminosity will generate electromagnetic fields at the collision point that will be strong enough to induce coherent disruption of the opposing beams as they pass through each other. Beam particles will be scattered as they pass through the interaction region, and will suffer significant loss of energy as they radiate high-energy photons (called beamstrahlung). These effects may require that the beams cross each other at finite angles in order to prevent the enlarged out-going beams from striking the final focusing elements of the machine. They may also generate a large spread in the distribution of center-of-mass energies of the colliding particles. While beam-beam disruption and beamstrahlung are present and observable at the SLC (observation of beamstrahlung photons is, in fact, a useful diagnostic tool), neither will impact physics studies in any significant way.

3.1 Goals for Machine Performance

The total visible e^+e^- hadronic cross section is shown in Fig. 1. With radiative corrections the peak at the Z° is about 30 nb, so an average luminosity of 10^{27} cm^{-2} sec^{-1} will yield ≈ 300 events in 10^7 sec (≈ 3 months of accumulated operation). It appears that a reasonable goal for the first year of machine operation should be an average luminosity of a few 10^{27} cm^{-2} sec^{-1}, and that eventually luminosities should exceed 10^{30} cm^{-2} sec^{-1} to fully explore the particle physics in this mass range.

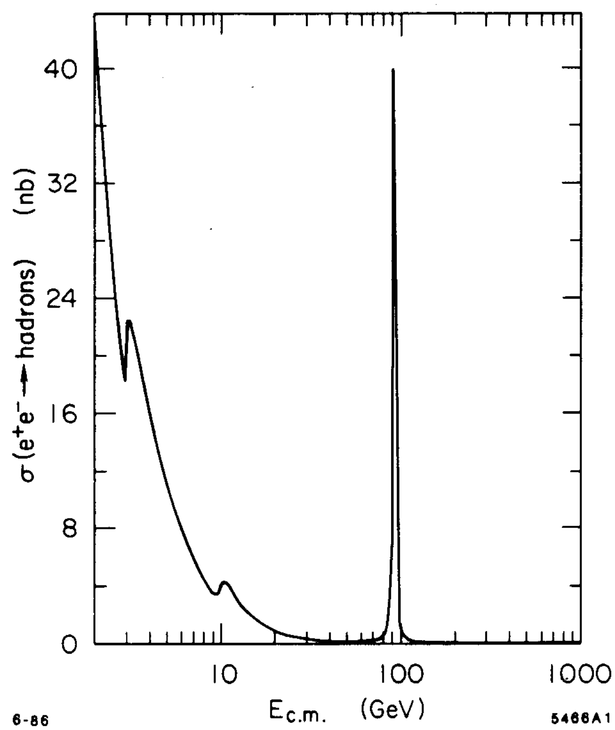

Fig. 1. The total e^+e^- hadronic annihilation cross section without initial state radiative corrections.

4. THE SLC MACHINE

The goals put forth in the previous section will certainly be achievable at center-of-mass energies of 80–200 GeV by ever larger e^+e^- storage rings. The design luminosity of the LEP machine at CERN (30 km in circumference) is above 10^{31} cm^{-2} sec^{-1}, and the community looks forward to the beginning of the experimental physics program there in late 1989 or early 1990. The SLC, shown in Fig. 2, is a somewhat more risky proposal. The Concept Design Report[3] for this machine was released in 1980, funding was approved in 1983 and initial luminosity was achieved at the interaction point this past Summer.

Bunches of electrons and positrons are simultaneously accelerated to high energy in the SLAC linac, deflected into separate ARC transport lines which bring them into opposition to each other, focused to small transverse dimensions and brought into collision at a single interaction point (IP). The bunches are discarded after they have passed through the IP once. This cycle is repeated up to 180 times per second. The design machine parameters and corresponding goals for initial running are summarized in Table I. Values that have been achieved in practice so far are also given in the table.

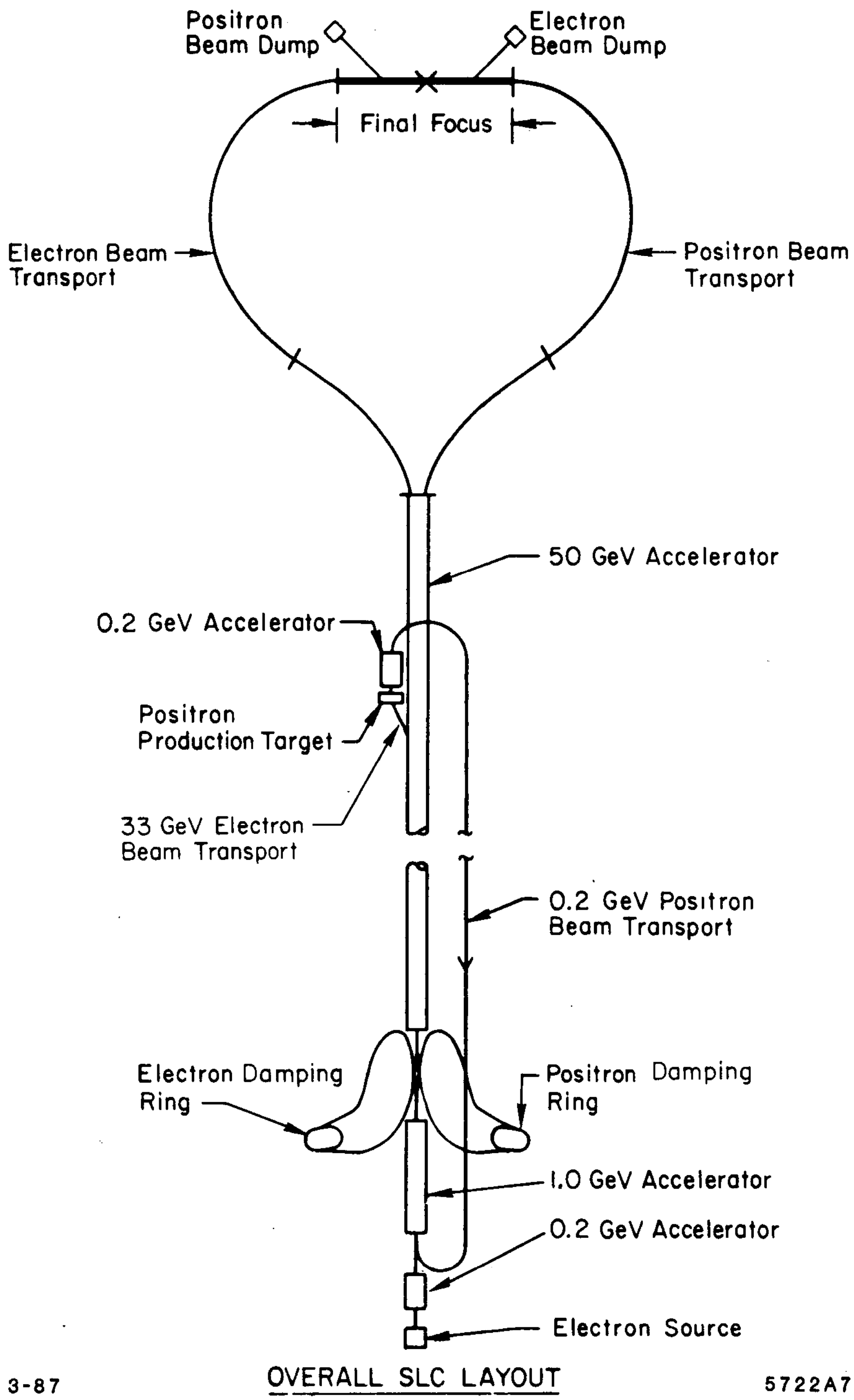

Fig. 2. Layout of the Stanford Linear Collider.

Table I. SLC machine parameters.

Parameter	Design	Initial Goal	Achieved[a]
Energy (GeV)	50	46	53
Intensity ($e^{\pm}$/pulse)	7×10^{10}	1×10^{10}	1×10^{10} (e^+)
			2×10^{10}(e^-)
Spot sizes (σ in μm)	1.7	4	5 (horizontal)
			3 (vertical)
Repetition rate	180	60	30
Luminosity ($cm^{-2}s^{-1}$)	6×10^{30}	10^{27}	$\sim 10^{26}$

[a]These values have been reproducably achieved, but not simultaneously with good efficiency.

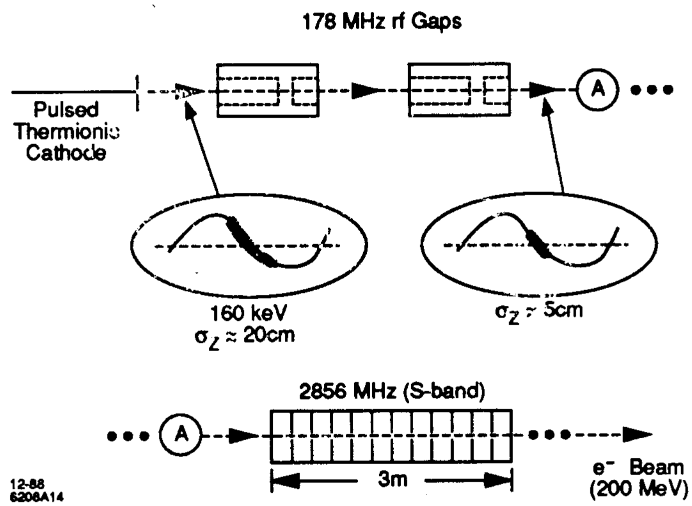

Fig. 3. Conceptual sketch of bunch compression in the SLC e^- source.

4.1 Electron Source

The operating cycle of the SLC begins when two bunches of electrons are generated 58 nsec apart from a pulsed thermionic cathode. The first of these bunches will eventually be transported to the IP to collide with a bunch of positrons, while the second (the so-called "scavenger bunch") will create positrons to be used in the next machine cycle. A schematic illustration[4] of the initial compression and acceleration of the electron bunches is shown in Fig. 3. The thermionic gun produces 20–cm-long bunches of nonrelativistic electrons (kinetic energy $\approx$ 160 keV) that cannot be captured by the 2856 MHz S–band (10 cm) base frequency of the main accelerator RF.

The bunch length is compressed by two RF gaps operating a subharmonic of the 2856 MHz and phased with respect to the gun pulse to introduce a velocity profile within each bunch that is correlated with longitudinal position. Following each RF gap there is a drift space of 1 m that allows the bunch to compress as the more energetic particles at the tail of the bunch catch up with the less energetic particles at the head of the bunch. After the second drift space the bunch length has been reduced to 5 cm, at which point it is sufficiently short to fit into one S-band RF bucket so further compression and acceleration to relativistic velocities is done in a single 3-m section of linac waveguide. Acceleration to 200 MeV then occurs in the first section of the main accelerator (actually called Sector 0).

The two electron bunches are joined by a single bunch of 200-MeV positrons that was created on the previous cycle of the machine, and the three bunches are accelerated to 1.2 GeV in Sector 1 of the linac. The electron source is fully operational and meets SLC specifications. Pairs of electron bunches with intensities greater than 7×10^{10} per bunch can be generated and captured within the acceptance of the first stage of the linac.

4.2 Damping Rings

It is necessary to use a pair of small storage rings[5] to compress the transverse phase space of the bunches created by the electron and positron sources. The two electron bunches are transported to one ring where their horizontal and vertical emittances,

$$\epsilon_{x,y} \equiv \sigma_{x,y} \times \sigma_{x',y'} \quad , \tag{4}$$

are reduced by radiation damping. (See Fig. 4.) Measured damping times for the electron ring are shown in Fig. 5. Energy lost as synchrotron radiation emitted by beam particles as they pass through the magnetic elements of the ring is replaced by purely longitudinal acceleration in the RF cavities of the ring. Quantum fluctuations in the energies of the emitted photons limit compression of the phase space. Dispersion in the dipole bend magnets causes shifts in the central orbits of particles as they emit photons and results in larger equilibrium emittance in the horizontal plane than in the vertical plane. In the SLC rings, quantum mechanical equilibrium is reached in both planes in less than 10 msec (suitable for 120 pps operation), and equilibrium levels are well below that required to achieve SLC design luminosity.

When the data shown in Fig. 5 was taken, the rings were being operated with the vertical and horizontal betatron tunes uncoupled. The standard procedure to eliminate the difference between the equilibrium values of ϵ_x and ϵ_y is to adjust the horizontal and vertical betatron tunes of the ring to an integral difference. The betatron motions of particles in the two planes are then coupled by imperfections in the ring lattice so that $\epsilon_x = \epsilon_y$, and both reach the design value in the same length of time. This is now routinely done.

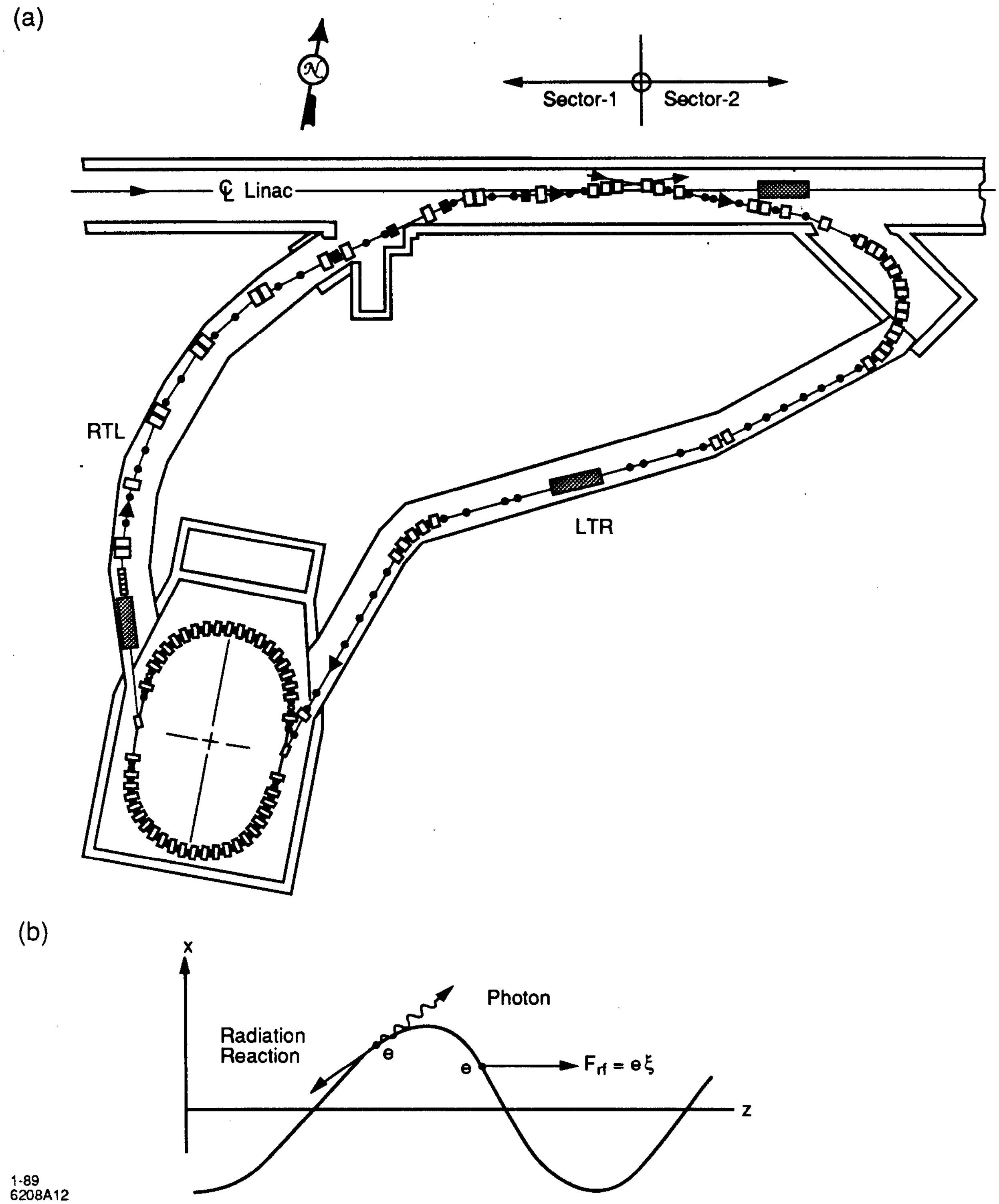

Fig. 4. (a) SLC damping ring with associated linac-to-ring (LTR) and ring-to-linac (RTL) transport lines. (b) Illustration of the mechanism responsible for radiation damping of the transverse phase space of beams stored in the ring. Particles will radiate strongly as they pass through the magnetic elements of the ring. The energy lost to synchrotron radiation is replenished by an externally-applied RF field which has small transverse components.

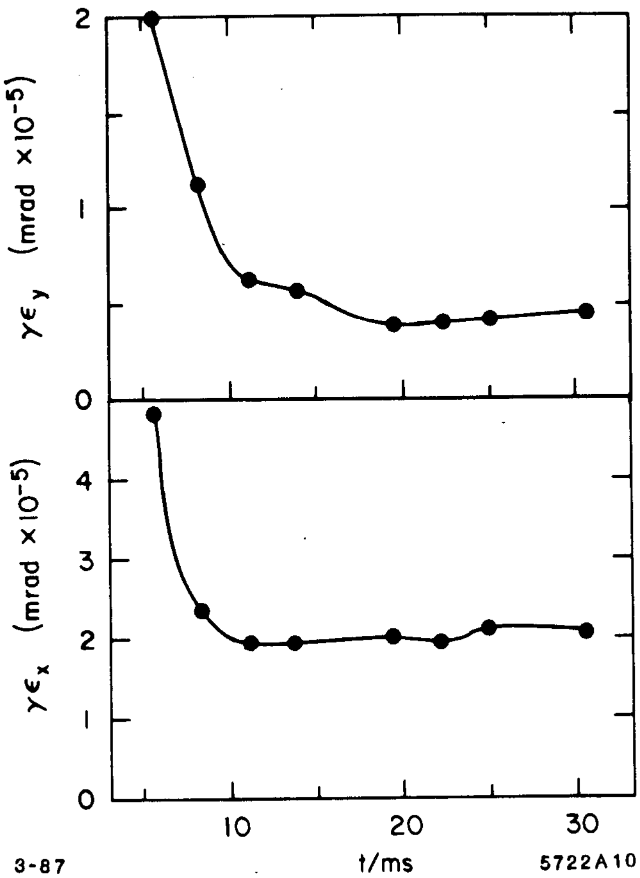

Fig. 5. Measured damping times in the e^- damping ring. The design of the SLC requires that the invariant emittance of the beam ($\gamma \times \epsilon$) be reduced to 3×10^{-5} rad-m or less in both planes.

The transverse phase space occupied by the positron bunch is initially larger than that of the electron bunches, so it must be damped for a longer period of time. To account for this, the positron bunch that is injected into the damping ring on a given cycle of the machine is left there until the next cycle, while a second bunch, created and stored on the previous cycle, is extracted, accelerated and transported to the IP.

The channel that leads from the damping ring back to the linac (RTL) is not just a passive transport line. A conceptual sketch of the dynamics of this line is shown in Fig. 6. It is necessary to restructure the longitudinal phase space of the beam as it leaves the damping ring before it can be accelerated in the linac. The damping rings were designed to produce an equilibrium bunch length $\sigma_z \approx 6$ mm, with momentum spread $\sigma_p \approx 1$ MeV, while in the linac σ_Z must be maintained to 0.5–1.5 mm to avoid excessive instabilities due to transverse wake fields (discussed below). Compression of the bunch length in the RTL is accomplished by introducing a phase dependent momentum boost to the beam as it leaves the damping ring. A large dispersion is created in the remainder of the RTL so that particles at the head and tail of the bunch travel different distances to reach the linac. This results in the desired reduction in the bunch length, and the growth in the energy spread of the beam is only about 10 MeV, which is small compared to that generated during the acceleration process in the linac (discussed below).

Unfortunately, the vacuum chambers of the damping rings contain rapid transitions in radius that create turbulence in the beam and wake potentials that increase the equilibrium bunch length as the beam intensity is increased. The measured bunch length is shown in Fig. 7 for various beam currents. At intensities greater than $\approx 3 \times 10^{10}$ particles per bunch the length becomes too great to be recovered by the RTL compressor. It is known how to correct the vacuum design, but the pipe will have to be rebuilt and, at the present time, this is a limitation on machine performance.

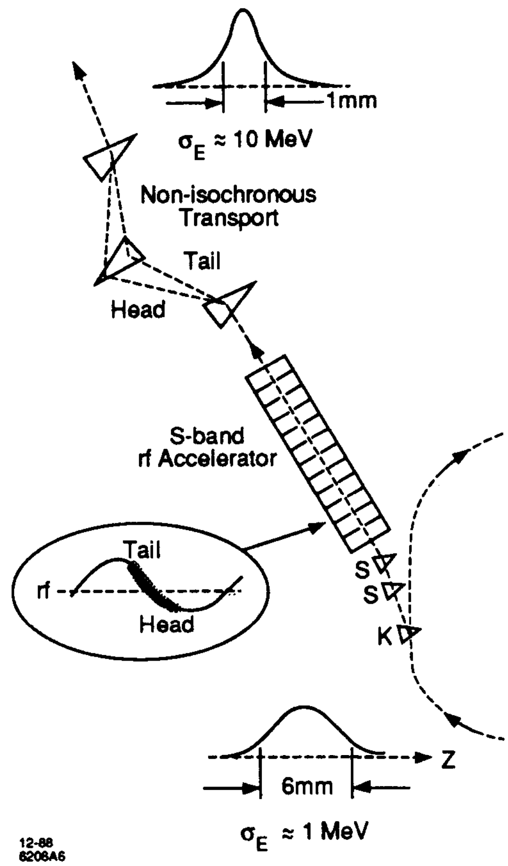

Fig. 6. Conceptual sketch of bunch compression in the RTL transport line.

4.3 Linac

To build the SLC it has been necessary to increase the energy of the linac from 32 GeV to 50 GeV and also to increase the accelerated charge from 10^9 to 5×10^{10} particles per bunch.[6] The corresponding increase in RF power has been realized by upgrading the linac with over 200 new 67 MW klystron tubes. Beam energies of 53 GeV have been achieved and the machine is routinely operated at 46 GeV.

The dramatically increased bunch intensities and reduced emittances have required that extreme care be taken to understand and control the effects of the interactions between individual particles within each bunch and between the particles in

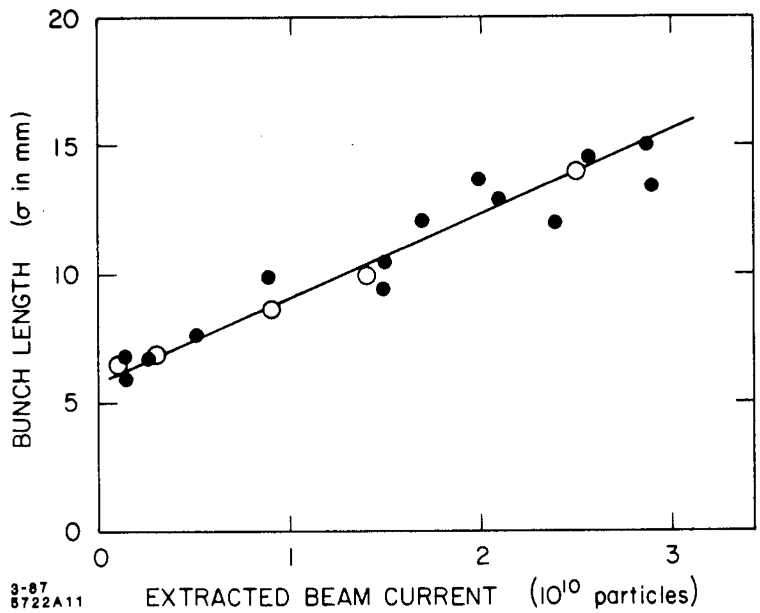

Fig. 7. Measured values for the equilibrium bunch length in the e^- damping ring as a function of extracted bunch population. The design length is 6 mm, and should be independent of population.

the bunch and the accelerating structure of the linac. Growth in the energy spread of the beam and distortions in the bunch shape generated by longitudinal and transverse wakefields have been controlled by installation of additional focusing elements in the first three sectors of the linac, upgrades to the beam position monitoring hardware (BPMs), improvements in beam steering algorithms, implementation of new and previously untried RF phase configurations and by the establishment of suitable feedback networks.

4.3.1 Wakefields in the SLAC linac. As a high-intensity bunch of electrons (or positrons) travels through the disc-loaded accelerating structure of the linac, forces are exerted on individual particles not only by the externally generated RF field but also by the remaining particles in the bunch and their image currents in the metalic structure. A complete calculation of the retarded electromagnetic potential at the location of each particle in the bunch requires fairly extensive computer code but most of the qualitative features of these wakefields can be grasped from the simple quasi-static picture in Fig. 8. A test particle some distance behind a charge element q will be deaccelerated by the residual longitudinal force created by q and its image charges, and if the charge element is not at the center of the waveguide there will be, as well, a net transverse force on the test particle. For small transverse displacements (r << a), the strength of these wake fields can be written in terms of potentials that depend only on the longitudinal separation of the two charges:

$$F_L = q \times W_L(l) , \tag{5a}$$

$$F_T = q \times (\frac{r}{a}) \times W_T(l) . \quad (5b)$$

The results of detailed calculations[7] of W_L and W_T for the SLAC accelerating structure are shown in Fig. 9. This represents the interaction between particles at the head of the bunch and those at the tail of the bunch so it is clear that as the accelerated bunch is made shorter, the longitudinal force excerted on particles at the tail of the bunch increases. This will cause the spread in the distribution of particle energies observed at the end of the linac to grow. On the other hand, the transverse force on the tail of the bunch grows as the bunch length increases over the range of distances of interest (few millimeters). This will distort the bunch shape in ways that are not repairable later in the Final Focus System (FFS). There are methods to control the effects of these wakefields.

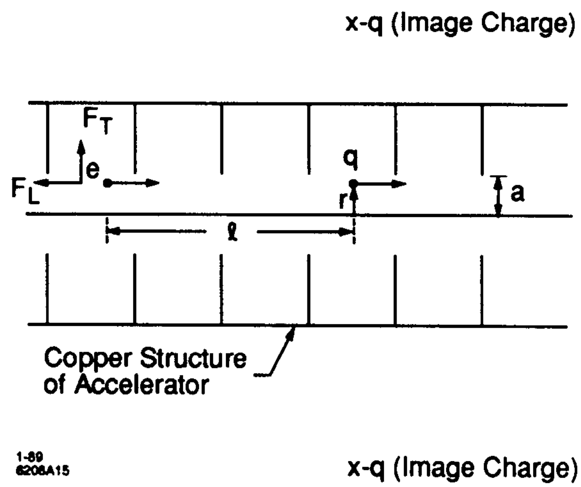

Fig. 8. Forces exerted on a test charge trailing a distance behind a charge element q by the charge element and its image charges in the disc-loaded copper accelerating structure of the SLAC linac. The test charge is taken to be the same sign as the charge element.

4.3.2 Energy and energy-spread in the linac. When the beam intensity exceeds $\approx 10^{10}$ particles per bunch, the longitudinal head-tail interaction will generate an excessively large energy spread in the beam. At 5×10^{10} particles per bunch, the difference in energy between particles at the head of the bunch and those at the tail would become as large as 2 GeV at the end of the linac (Fig. 10) if a bunch with $\sigma = 1$ mm is placed on the crest of the RF wave. This can be compensated for by placing the bunch ahead of the RF crest so that the external field is larger at the tail than at the head, but this must be done quite accurately. The minimum in the energy spread is only a few S–band degrees wide.[8] (See Fig. 11.) The RF phase can be adjusted with this precision but corrections must be continuously applied to account for long-term instabilities created by temperature and pressure drifts in the RF cavities and the gas-filled timing cables that run the entire length of the linac.[9] In practice, the energy spread of the beam is maintained with $\sigma_E/E \approx$ 0.2–0.3%.

4.3.3 Transverse wake distortion and BNS damping.

It is clear that distortions in the bunch shape due to the transverse wakefield can be minimized by maintaining the beam trajectory as near to the axis of the waveguide as possible (Eq. 5b). A typical linac orbit is shown in Fig. 12. The BPM system in the linac, combined with presently used steering algorithms, are sufficient to simultaneously place both the e^- and the e^+ beams within a quarter of a millimeter (rms) of the center of the guide in both transverse planes over the entire length of the linac (3 km). The effects of deliberately mis-steering the beam are shown in Fig. 13. The well-steered beam in the middle of the figure shows little distortion in the bunch shape, but if a betatron oscillation is induced with a dipole steering magnet at the beginning of the linac, then by the time the beam reaches the end of the linac, the tail is displaced laterally with respect to the head by many times the intrinsic width of the bunch.

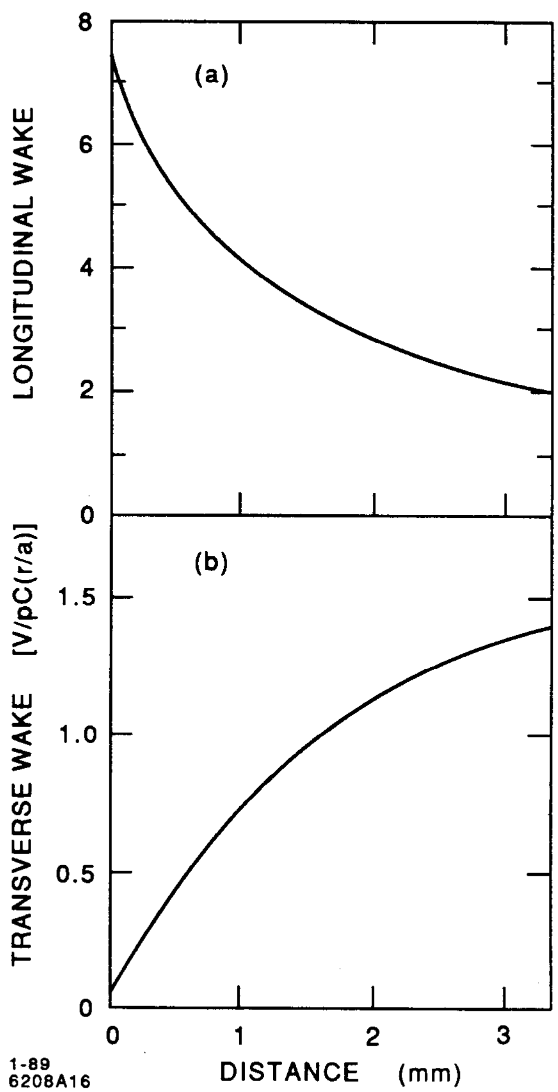

Fig. 9. Wake potentials calculated for the SLAC accelerating structure. (a) Longitudinal wake, and (b) transverse wake.

The development of the transverse head–tail distortion in the linac is coupled to the energy distribution of particles in the bunch in a nontrivial manner. If there were no correlation between the energy of a particle and its longitudinal position in the bunch then, as depicted in Fig. 14, any residual coherent betatron oscillation in the beam trajectory that might be induced by steering errors will result in repeated (coherent) transverse kicks to the tail of the beam. This coherence can be destroyed if the energies of particles at the tail of the bunch are made to be systematically different from the energies of the particles at the head, so that the betatron wavelengths of

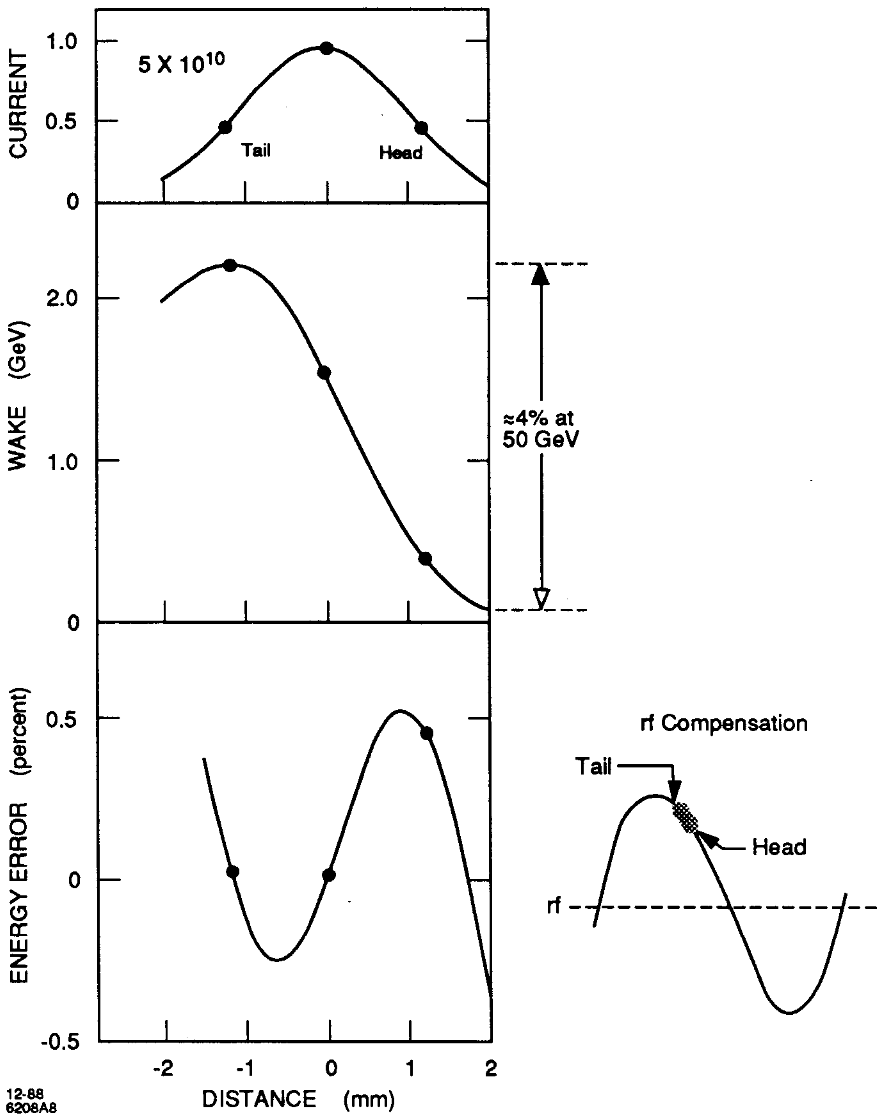

Fig. 10. RF compensation of the accumulated longitudinal wake potential in the linac. (a) Bunch longitudinal density profile with $\sigma = 1$ mm. (b) Energy deficit observed at the end of the linac for a bunch accelerated at the peak of the RF crest. (c) Energy error with respect to the center of the bunch observed at the end of the linac for a bunch accelerated 10° ahead of the RF crest.

their orbits are not the same. This can be accomplished by adjusting the phase of the linac RF so that the bunch is not placed exactly at the peak accelerating voltage. If the beam is placed behind the RF crest for part of the length of the linac and then shifted to be ahead of the crest for the remainder of the acceleration cycle, then a situation can be realized in which all particles will have undergone the same

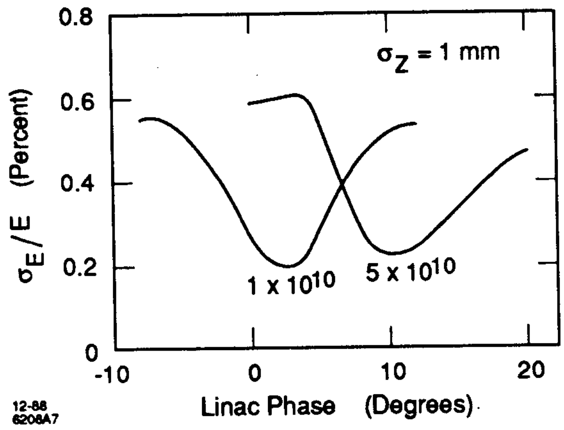

Fig. 11. Energy spread observed at the end of the linac for 1-mm-long bunches of various intensities as a function of the bunch phase with respect to the RF crest. One degree of RF phase corresponds to ≈ 1 psec of time.

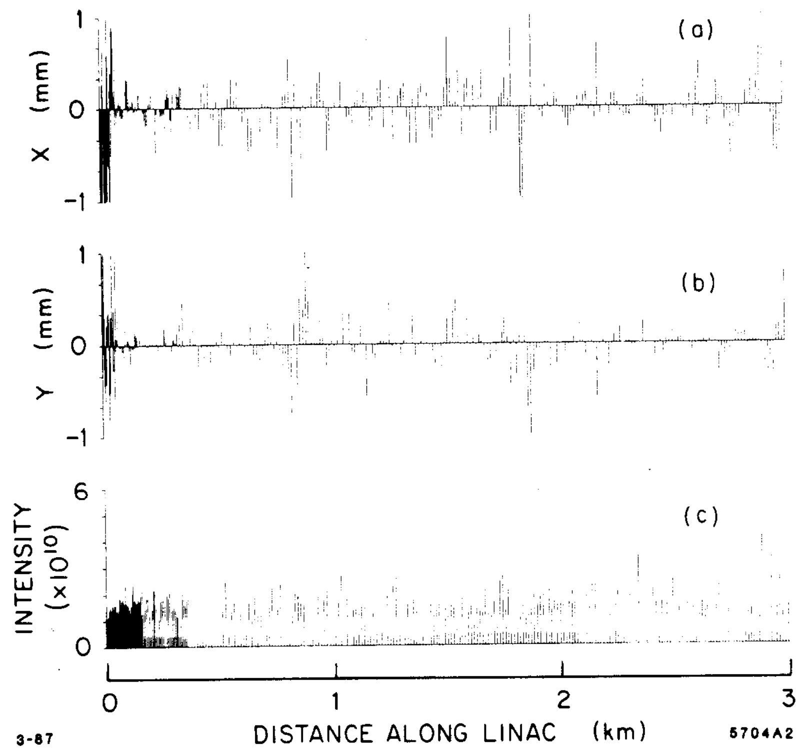

Fig. 12. Horizontal and vertical orbits in the SLAC linac. The displacement of the beam from the nominal centerline of the accelerator is measured at over 200 locations along the 3 km length of the machine. Each measurement is plotted in the figure as a vertical line. Positive offsets are displayed by lines that extend above the axis and negative offsets by lines that extend downward. The full scale corresponds to offsets of ±1 mm, and the rms deviation of the 232 measurements is approximately 0.25 mm in both planes.

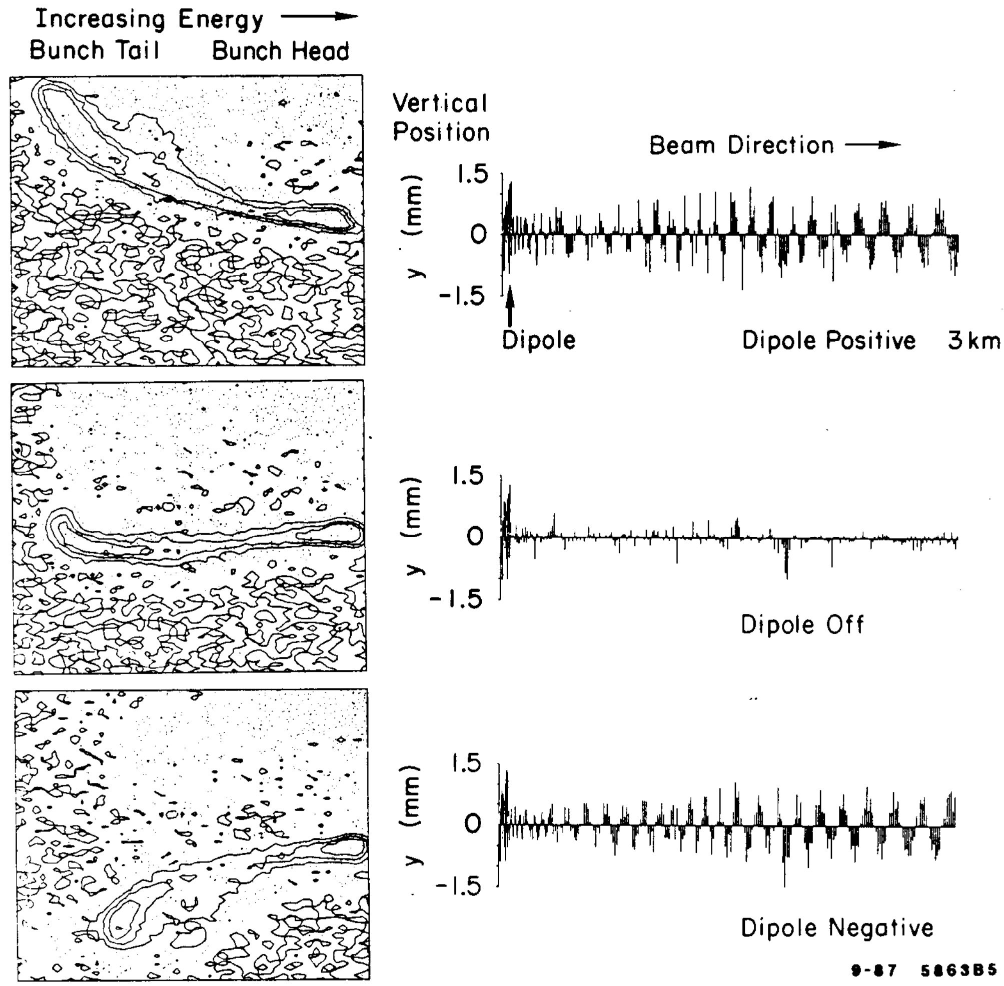

Fig. 13. Effect of deliberately mis-steering the e^- beam in the linac. The pictures at the left side of this figure are measured contour plots of the bunch population projected into the yz plane. The tail of the bunch (far left in the contour plot) is seen to be severely deflected with respect to the head when the beam is not maintained on axis in the accelerating structure.

net acceleration at the end of the linac, but at no other point along its length. This technique is known as Landau damping. A generalization of this idea (BNS damping[10]) takes advantage of the fact that the effective focusing strength of the linac quadrupoles is greater for lower energy particles. It is possible to partially offset the transverse wake forces with the external quadrupole fields by choosing to place the beam behind the RF at the beginning of the linac where the effect of the transverse wake is greatest. This scheme has been successfully used in the SLAC linac to control the growth of transverse instabilities in the beam for bunches with 2–3 $\times 10^{10}$ particles per pulse. The increase of the bunch length in the damping rings has prevented tests of these techniques at higher currents.

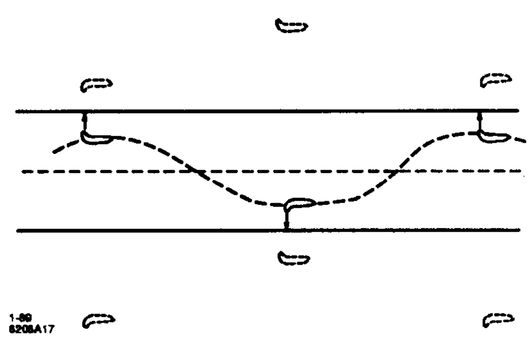

Fig. 14. Transverse wake forces on the tail of a bunch as it travels down the linac with a betatron oscillation of finite amplitude.

The detailed pattern of klystron phases is chosen to achieve both an acceptable energy spread and to provide control of transverse wake instabilities.

4.3.4 Linac feedback. Feedback loops are used[11] to control the energy of the beams produced by the linac and to monitor the energy spread of the beams. Additional loops are used to maintain constant trajectories for each beam through the machine by controlling the position and angle of the beam orbit at the point of launch into the linac at the end of the RTL, and again at the point of launch into the ARCs at the end of the linac.

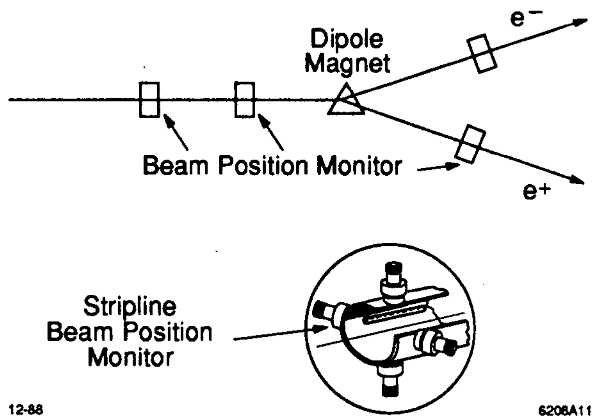

Fig. 15. Beam energy measurement in the beam switch yard. A stripline BPM is shown in the insert. Signals induced on four electrodes place symmetrically about the centerline of the BPM are individually read out and used to measure the location of the beam with respect to the electrical center of the device.

The beam energy is measured at the end of the linac with beam position monitors upstream and downstream of the dipole bend magnet that separates the e^- and e^+ bunches in the Beam Switch Yard (BSY). (See Fig. 15.) This system forms a spectrometer that can be read out on each pulse of the machine by a distributed microprocessor network. The single-pulse resolution of this spectrometer is $\sigma \approx 25$ MeV, but the absolute scale is not well determined. (Precise spectrometers, located in the extraction lines of the FFS have been used to set the absolute energy scale of the machine.) The net acceleration of the beams is controlled without change to the energy spread by simultanously adjusting the RF phase of a pair of subsections of the linac as shown in Fig. 16. Examples of the stability of the energy of the e^- beam with and without feedback control are shown in Fig. 17.

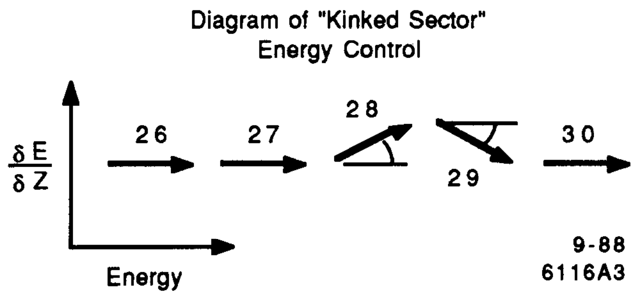

Fig. 16. Phase diagram represention of the summation of the contribution to the beam energy of a series of klystrons. The beam energy is controlled by advancing the phase of one set of klystrons and simultaneously retarding the phase of an adjacent set. Note: This figure is not explicitly correct in that it does not include the pattern of phases that would be imposed to minimize the beam energy spread and to affect BNS damping.

The energy-spread of each beam is monitored in the BSY at a location where the horizontal dispersion is large. Each beam is "wiggled" in the vertical plane by a special magnet with a dipole field that alternates direction along its length. (See Fig. 18.) The horizontal width of the swath of synchrotron radiation emitted as the beam passes through this wiggler magnet is proportional to the energy-spread of the particles in the beam, and can easily be monitored with a suitably-placed profile monitor viewed by a TV camera with a digitized rastor. This signal is not presently built into an automated feedback loop but is used as a visual monitor.

The use of feedback to make fine adjustments of beam trajectories and machine timing systems is very much at the heart of the operation of the SLC. This function occurs, for the most part, naturally in a well-designed storage ring in which only those particles that follow stable orbits survive; but in a single-pass machine such as the SLC, the beam is new on each pulse. There will certainly be more of these loops as smaller spots of more intense beams are maintained in collision at the IP.

4.4 The Positron Source

The scavenger e^- bunch is removed from the linac at a point two-thirds of the way down its length (after acceleration to $\approx$ 33 GeV) and is steered onto a water-cooled target. Low energy positrons generated in electromagnetic showers in the target are collected by a tapered solenoid and accelerated to 200 MeV. (See Fig. 19.) A transport line returns the e^+ bunch to the beginning of the first sector

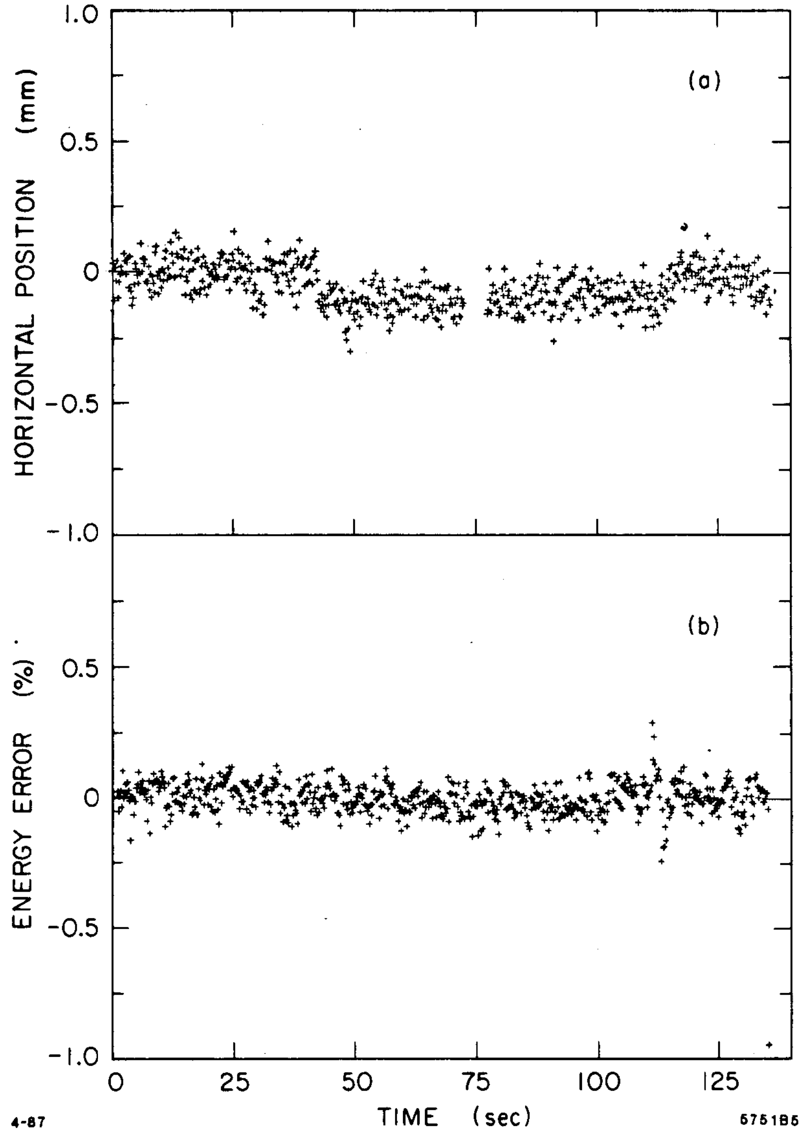

Fig. 17. Pulse-to-pulse measurements of the e^- beam. (a) Without feedback control, and (b) with feedback control.

of the linac, where the beam is accelerated to 1.2 GeV before being injected into the South Damping Ring. It is possible to tune[12] the positron source to generate 10^{10} e^+ at the end of the linac with 2–3 $\times$ 10^{10} electrons incident on the production target but it is more typical to obtain a somewhat smaller yield. Power absorption limitations in the existing production target prevent use of scavenger bunches with appreciably greater intensities.

4.5 ARCs and Final Focus

A number of mechanical difficulties that plagued the ARC transport lines during early commissioning have been overcome sufficiently well that they no longer are

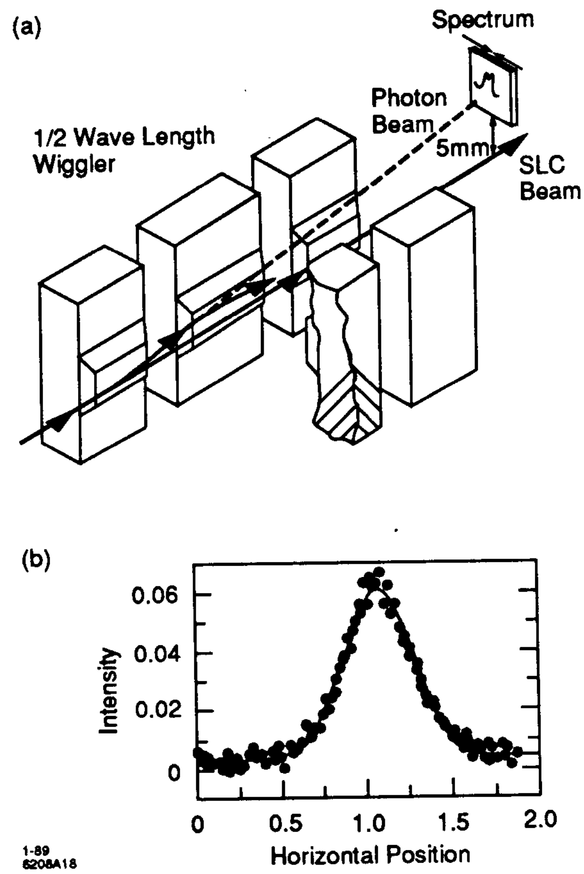

Fig. 18. Measurement of the beam energy spread in the BSY. (a) Conceptual illustration of the wiggler magnet and profile monitor screen used to make the measurement, and (b) example of the digitization of the TV rastor scan of the light intensity from the profile monitor. The width of the distribution is proportional to the beam energy spread. The data correspond to $\sigma/E \approx 0.27\%$.

a limitation to machine performance.[13] Residual errors in the alignment and field gradients of the ARC lattice and in-beam steering generate cross-plane coupling (Fig. 20) that must be corrected in the FFS. This increases the complexity of the overall tuning procedure and if the horizontal and vertical emittances of the beam are not equal at the end of the linac, then coupling of the horizontal and vertical betatron orbits, which is phase dependent, will result in dilution of the smaller of the two-phase space areas. Continued work on the ARC optics has reduced these distortions to the point that no anomalous increase of the beam emittance occurs between the end of the linac and the beginning of the FFS.

The tasks assigned to the FFS[14] are to accept potentially distorted e^+ and e^- beams with finite momentum spread at the ends of the ARCs, to transform the phase space occupied by these beams to create a focus for each beam that is sufficiently

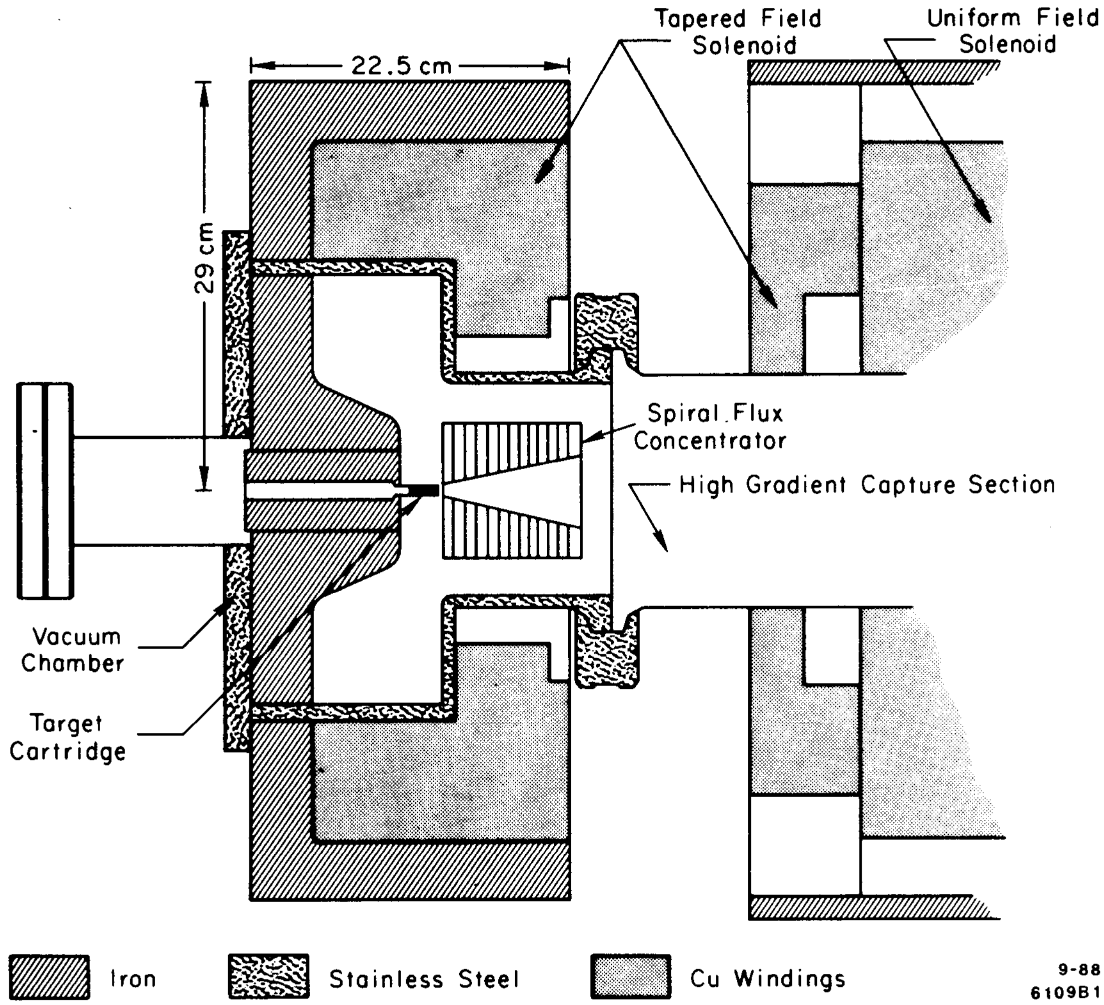

Fig. 19. Cross section of the positron target assembly.

small to generate luminosity, to do so at the unique point along the beamline at which the two opposing beams pass each other, to bring the two beams into collision and maintain them there and to transmit each beam outward along the beamline to its final dump. A schematic of the FFS optical elements is shown in Fig. 21. This system consists of four sections that must be tuned to yield the desired optical funtions at the IP. Notice that if the optics of the SLC beamline that starts at the exit of the damping rings and ends at the input to the FFS were constant, then it would be necessary to tune the FFS only once. The pulsed damping ring extraction magnets and the linac klystrons are not passive devices, however, and instabilities in their amplitudes and timings result in variations in the beam parameters at the input to the FFS. Drifts in power supplies and in diagnostic hardware and electronics also lead to variations in the parameters of the beam that must be corrected, either at their source or by retuning the FFS.

Adjustable quadrupoles paired with bend magnets in the most upstream section of the FFS (η-Matching, in Fig. 21) are used[15] to compensate the dispersion introduced in the beam by the bends of the ARCs. Measurements of the dispersion in the ARCs and FFS are made by varying the beam energy in the linac and recording changes of the beam orbit with stripliner BPMs. An example of a set of such measurements made before and after application of optical corrections is given in Fig. 22.

Using a pair of telescopic sections (First and Final Telescopes in Fig. 21), optical demagnification is achieved.[15] Quadrupoles with adjustable strengths located in these two sections allow the FFS lattice to be matched to the orientation and aspect ratio of the betatron beam ellipsoid presented at the end of the ARC. The darkened quadrupoles shown in Fig. 21 form, in effect, a "zoom lens" that is used to focus the beam to a proper waist at the IP. Quadrupoles in the First Telescope control the β-function at the waist, while the quadrupoles of the Final Telescope are used to match the location of the waist to the IP. Skew quadrupoles (shown as diamonds in Fig. 21) are used in conjunction with these telescopes to remove $x' \times y'$ and $x \times y'$ (and $y \times x'$) correlations (couplings) that might be present in the beam phase space. In principle it is necessary to have four skew elements to compensate all possible couplings but two are sufficient in the case of equal horizontal and vertical emittances.

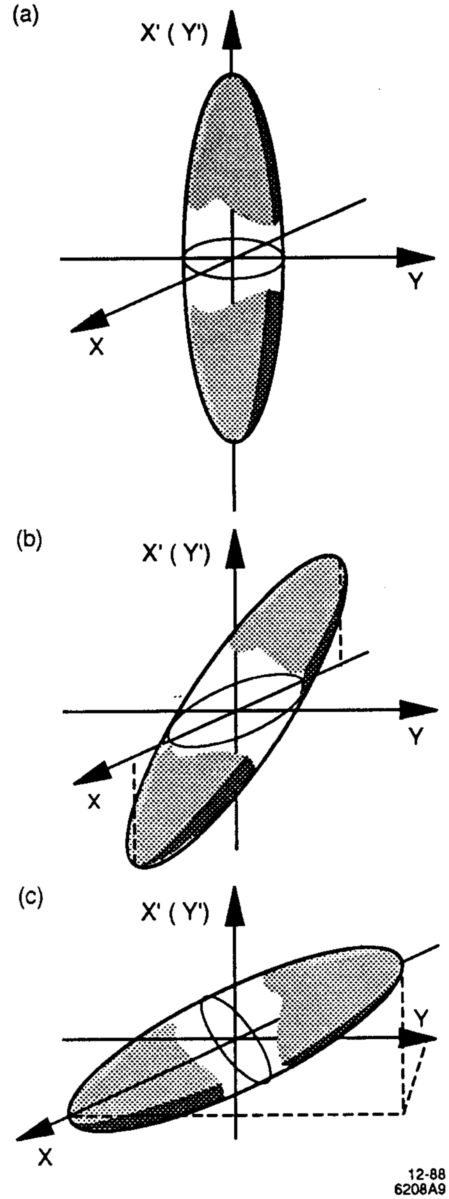

Fig. 20. Three-dimensional illustration of crossplane coupling. The transverse betatron phase space occupied by the beam is represented by an ellipsoid in four-dimensional space (x, x', y, y'). Three cases are shown: (a) an uncoupled focused spot, (b) an uncoupled unfocused spot, and (c) coupled phase space in which the projected areas in the (x, x') and (y, y') planes are both larger than in the case of an uncoupled beam.

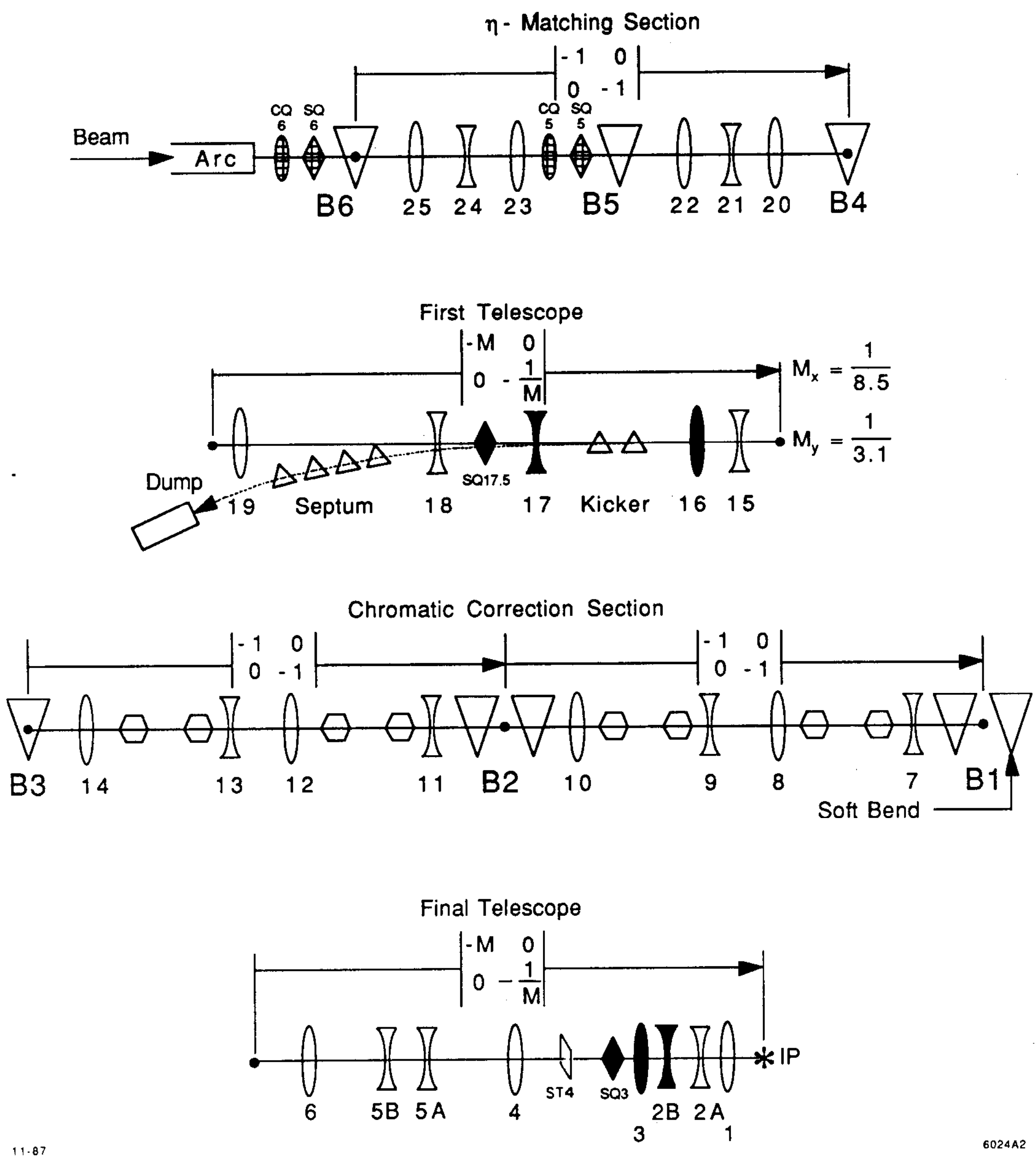

Fig. 21. Schematic of the FFS optics. The six variable quadrupoles used for adjusting the betatron phase space are shaded. The four quadrupoles used to correct the dispersion function are cross-hatched.

The telescopic system of the FFS will focus particles of a particular momentum at the IP, but the finite momentum spread of the beam will lead to chromatic dilution of the IP spot as particles of differing momenta are focused to differing points along the beamline.[16] (See Fig. 23.) The Chromatic Correction Section (CCS) located between the two telescopic sections is designed to correct the first-order chromaticity of the beamline. Dipole bend magnets horizontally disperse the beam in the local region of the CCS, so that sextupoles (magnets with quadrupole fields that vary

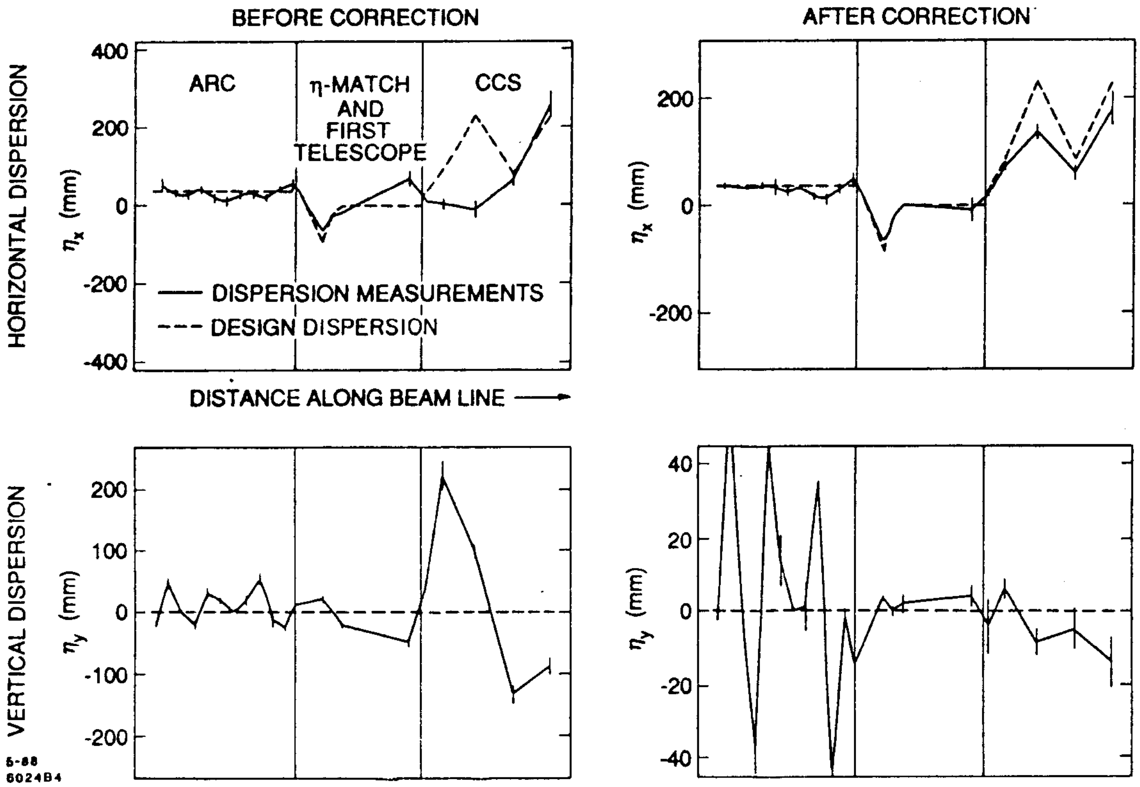

Fig. 22. Measurements of the horizontal and vertical lattice dispersion functions. at the end of the ARC and the beginning of the FFS. The measurements on the right-hand side of the figure were made after adjustment of the η-matching quadrupole strengths in the FFS. Note the change of scale with respect to the plots shown on the left-hand side of the figure.

Fig. 23. Illustration of the origin of chromatic dilution of the IP spot size. The solid lines indicate orbits of particles with nominal momentum p_0, while the dashed lines are orbits for particles with momenta $p_0 + \delta p$.

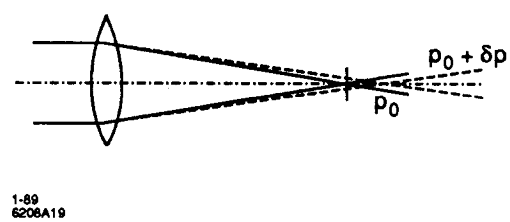

quadratically with distance from the centerline) can be used to provide momentum-dependent focusing strengths which can be adjusted to compensate the spread in focusing strength of the remainder of the FFS. The importance of this correction is shown[17] in Fig. 24. If the momentum spread of the beam were zero, then as the focusing strength of the FFS telescopic sections is increased (β^* made smaller) then the beam size will be reduced as

$$\sigma_{x,y}^2 = \epsilon_{x,y} \times \beta_{x,y}^* , \tag{6}$$

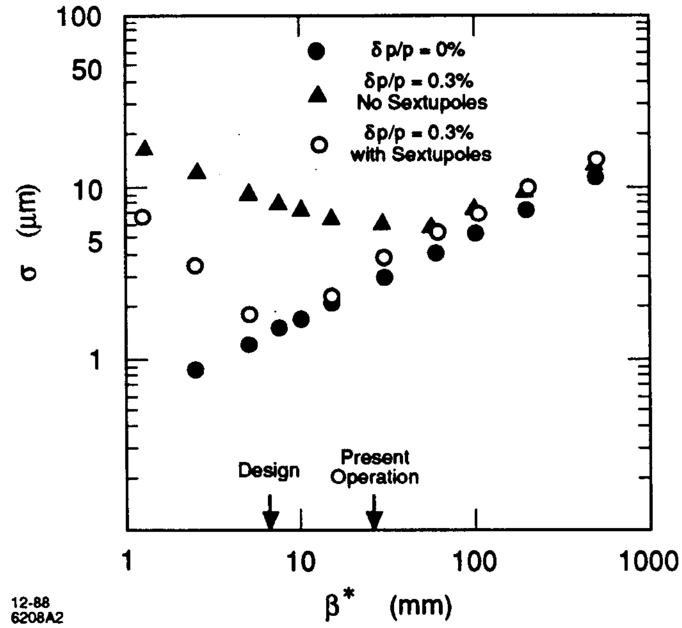

Fig. 24. Calculations of IP spot size as a function of the β-function at the IP. The emittance of the beam was taken to be 4 × 10^{-10} rad-m for these calculations and the dispersion of the beam at the IP assumed to be zero.

where β^* is the value of the β-function of the lattice at the IP. This is shown as solid points in Fig. 24. The effect of the finite momentum spread of the beam in the absence of chromatic correction and zero dispersion at the IP is also shown. As the telescopic demagnification is increased to reduce β^* the size of the beam in the final lens is increased and the induced chromatic aberrations grow. These aberrations dominate the spot size below $\beta^* \approx 50$ mm. The properly corrected spot size, shown as open circles in the figure, passes through a minimum of $\sigma \approx 1.7$ μm at $\beta^* \approx 7$ mm. Operation has been limited to β^* of 30 mm or larger primarily by backgrounds created in the final quadrupoles that are made worse as β^* is reduced (see below). Improved beam collimation and background suppression is presently being installed that will allow further reduction in β^*.

The beam intensity profile is measured at the IP by magnetically scanning the beam in steps as small as 1 μm across one of three fine carbon filaments (4, 7, and 30 μm in diameter) mounted on a ceramic holder that can be inserted onto the beamline by air actuated bellows. The wire target hardware[18] is shown in Fig. 25. Separate sets of wires are used to measure horizontal and vertical profiles. Signals are generated in the wires by secondary emission (SEM) of electrons from the carbon material, and by the emission in the far-forward direction of bremsstrahlung photons by the beam as it passes through the wire. Both of these processes are detected and used to determine the cross-sectional population of the particle density in the beam. Several examples of these profiles are shown in Fig. 26. The SEM signal

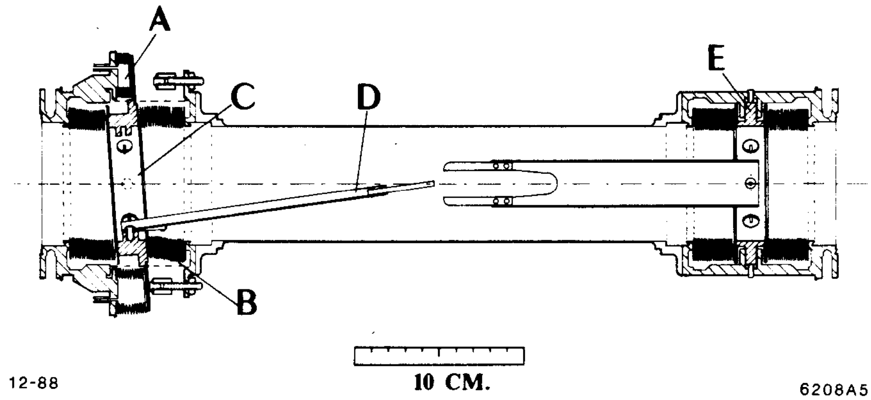

Fig. 25. Wire targets used to measure beam intensity profiles at the IP. Separate sets of wires are used to measure horizontal and vertical beam profiles. The wires are place ± 1.5 mm from the IP.

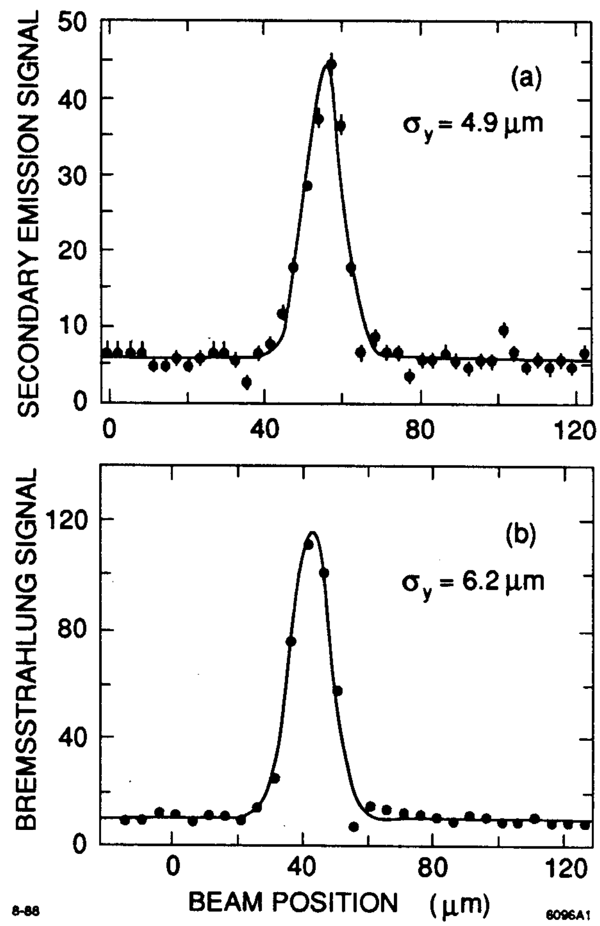

Fig. 26. Beam spot profiles. The observed forward bremsstrahlung signal is plotted as the beam is scanned across a 7 μm diameter wire in 4 μm steps. Steps as small as 1 μm can be used to measure beam profiles.

is determined not only by the number of particles that pass through the wire, but also by the intense electromagnetic fields generated by the remainder of the incident bunch. Emission of electrons from the wire is suppressed by the e^- cloud surrounding the wire and enhanced by the fields created by the e^+ bunch. The bremsstrahlung signals are more straightforward to interpret and are therefore most often used to determine the beam spot size.

Settings for the optical parameters of the FFS are determined in most cases by minimizing the individual beam sizes as measured by the wires at the IP. An example of such an optimization is shown in Fig. 27. Here the focal length of the final lens of the system has been varied and the beam size, measured at the IP, has been fitted to the expected behavior:

$$\sigma^2 = \epsilon \times \beta^* + \frac{\epsilon}{\beta^*} \times (\Delta f)^2 \quad , \tag{7}$$

Fig. 27. Optimization of the beam waist position. The parameter Δf represents a change of the focal length of the final lens of the FFS with respect to an arbitrary starting point. The beam size is measured at each step by magnetically scanning across the wire monitor at the IP and fitting a Gaussian function to the observed profile (Fig. 26).

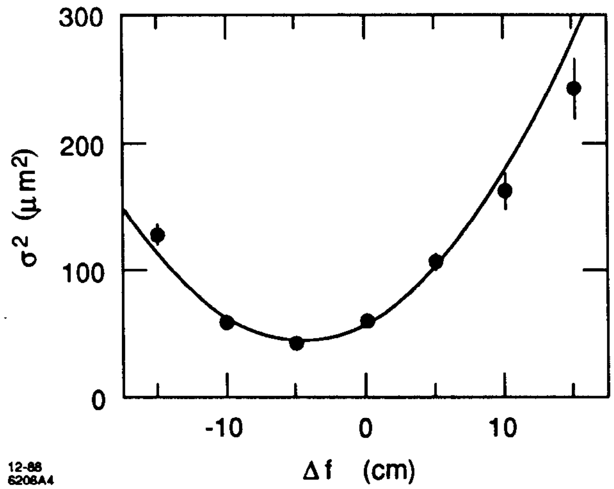

where $\epsilon \times \beta^*$ is the square of the beam size at the waist (Eq. 6) and ϵ/β^* is the square of the angular divergence of the beam at the waist. This type of scan is important not only because it determines the proper setting of the lens strength but also because it allows a determination of the emittance of the beam and the lattice β^*. Shown in Fig. 28 is a compilation of such measurements made with the e^- beam during a recent period of machine operation. Measurements of the horizontal and vertical emittance made simultaneously at the IP and at the end of the linac are in good agreement, as shown in the figure. This is important because it indicates that the optical corrections have been properly adjusted in the FFS and that the emittance of the beam is not overly diluted anywhere in the ARCs or FFS. (Quantum fluctuations in the synchrotron radiation emitted in the bends of the ARCs are expected to increase the emittance slightly, from 3×10^{-10} rad-m at the end of the linac to 4×10^{-10} rad-m at the IP.) Spot sizes of 5 μm by 3 μm (horizontal by vertical) are routinely produced at the IP.

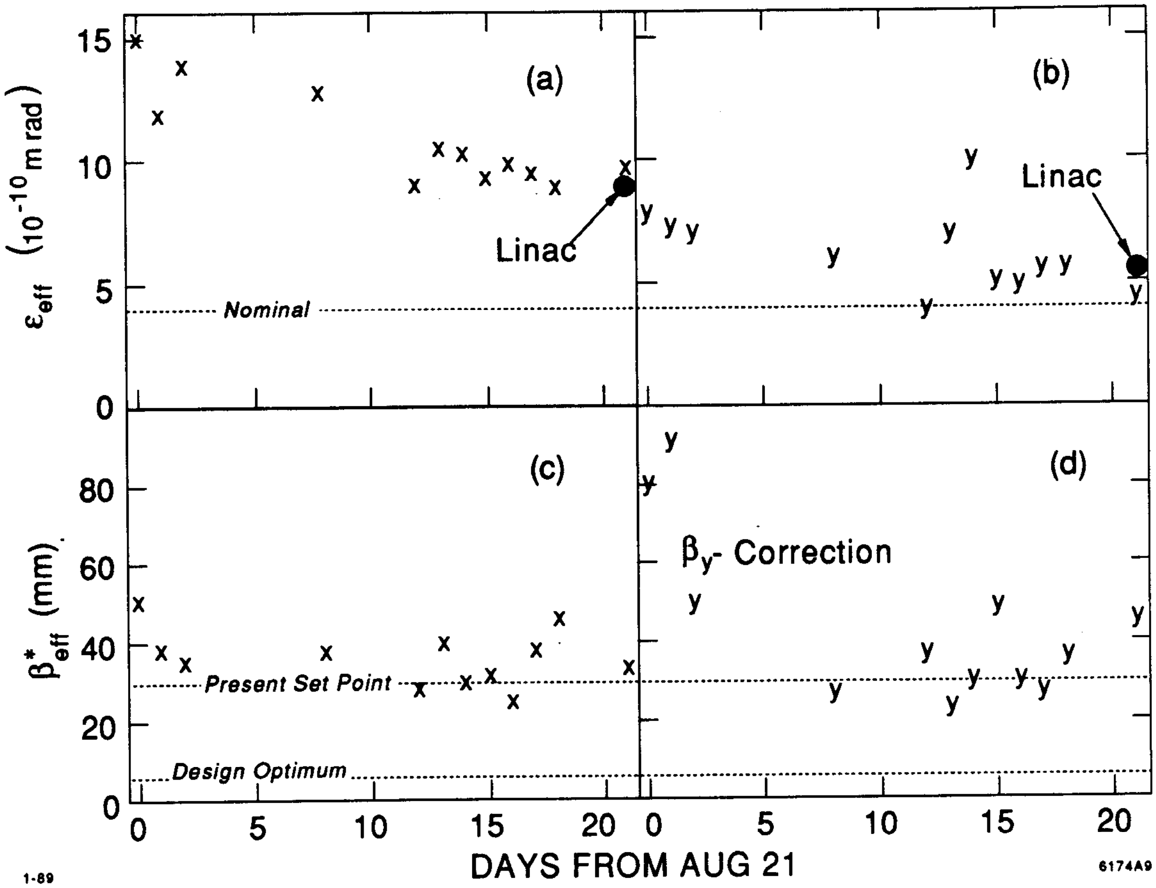

Fig. 28. Measurements of the e^- emittance and β^* observed at the IP. The results of measurements taken at the end of the linac are also shown. A correction to the vertical β-function was made early in this operating period to achieve $\beta^* \approx 30$ mm in both planes.

The production of small intense spots of electrons and positrons has made it possible to observe strong signals from the coherent interaction of the two beams. The deflection of one beam as it is scanned past the other, conceptionally shown in Fig. 29, is reconstructed on-line from measurements of the trajectory of each beam made with position monitors located inside the bore of the final lens magnets. Beamstrahlung photons emitted during the deflection of each beam are detected by a Čerenkov counter located downstream of the first bend in the outgoing orbit. Examples of these signals taken simultaneously from a single sweep of the e^+ beam across the e^- beam are shown in Fig. 30. Notice that the beamstrahlung flux is maximum when the beam undergoes maximum deflection and passes through a slight minimum when the beams are exactly aligned. The zero-crossing of the beam-beam deflection curve defines the precise location at which the two beams are properly aligned. On-line automated "push-button" software is used to sweep the beams past each other, measure the beam-beam deflection to determine the zero-crossing and to bring the two beams into collision. This procedure is sufficiently accurate to routinely maintain the beams in collision with their centers aligned to within 1 μm or better in both horizontal and vertical planes. Drifts in the beam–beam alignment have been

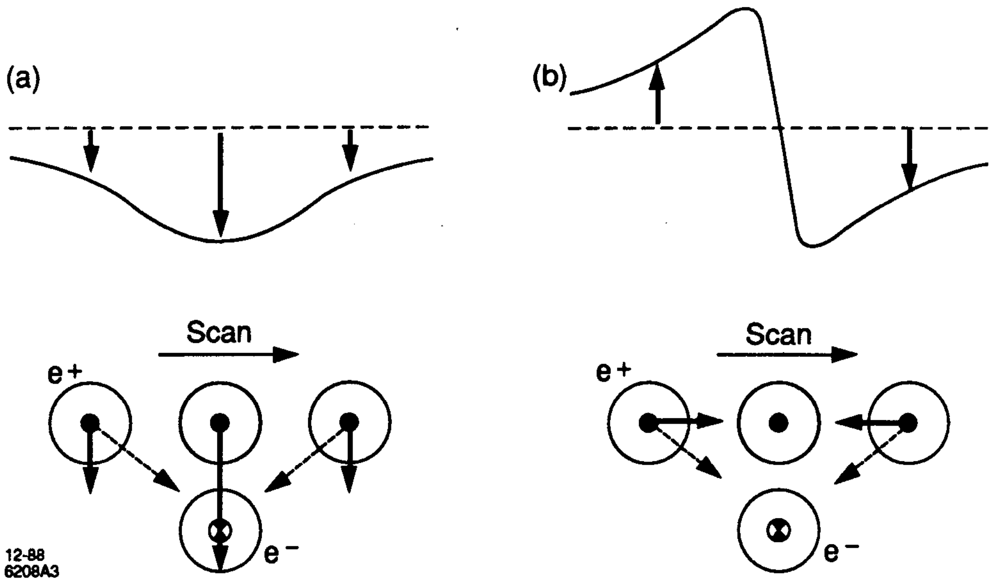

Fig. 29. The deflection of the e^+ *beam as it is scanned past the* e^- *beam. (a) The deflection in the plane perpendicular to the scan direction. (b) The deflection in the plane of the scan. When the beams are properly aligned, the deflection in the plane perpendicular to the scan will be zero, and the slope at the zero-crossing of the deflection in the plane of the scan will be a maximum.*

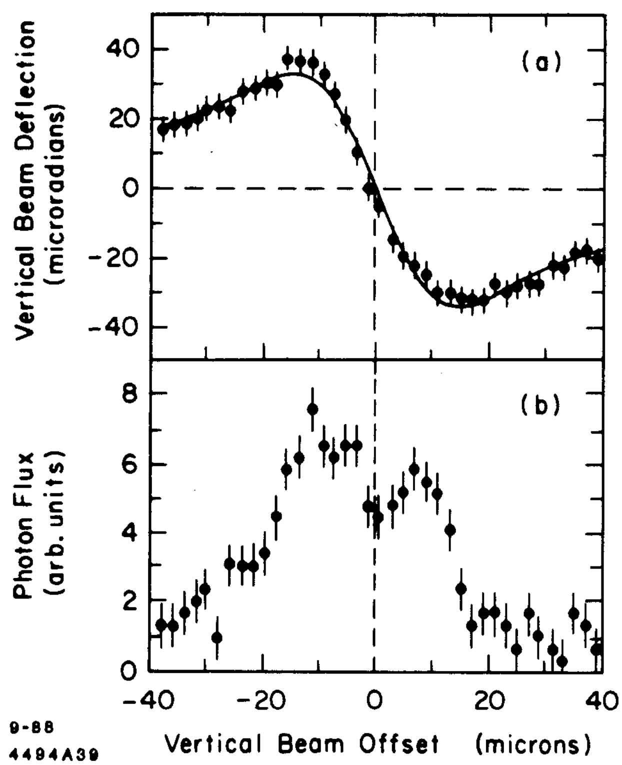

Fig. 30. Beam–beam deflection and beamstrahlung flux measurments taken simultaneously on a single scan of the e^+ *beam past the* e^- *beam.*

monitored and found to be small enough that they can be corrected with suitable feedback loops. An example of a three-hour history of the transverse position of the beam–beam interaction point determined with deflection scans is shown in Fig. 31.

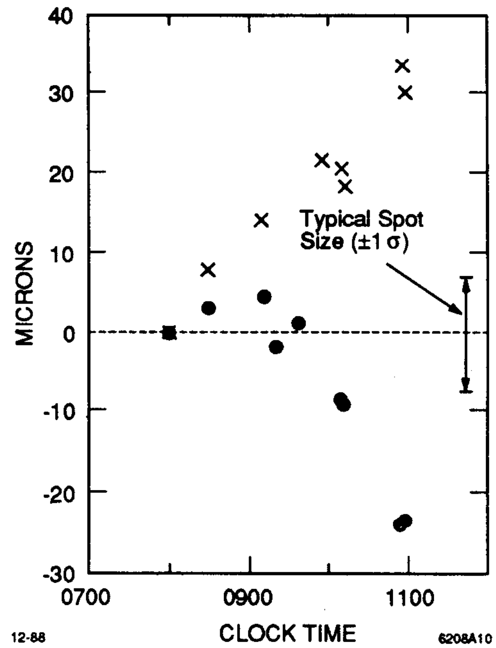

Fig. 31. Time history of the horizontal (x) and vertical (•) positions of the beam–beam interaction point as determined with deflection scans. The beam spot size was typically 6–7 μm while these data were taken.

4.6 Beam Collimation and Background Suppression

Electromagnetic debris, penetrating muons and slow neutrons that are created when stray beam particles strike apertures in the FFS constitute backgrounds that, if sufficiently intense, will make it impossible for the experimental detector at the IP to acquire usable data. Elimination of these backgrounds requires extensive shielding and protection of the detector and well-designed and implemented collimation of momentum and betatron tails of the beam phase space.

Soft electromagnetic particles (electrons and photons with kinetic energies of a few MeV) and slow neutrons that permeate the tunnels that contain the beamline components are prevented from entering the large IP detector hall by walls composed of concrete, lead and polyethylene. This shielding is sufficiently thick to reduce the residual flux of these backgrounds by two orders of magnitude. It is somewhat amusing to note that the duty factor of the machine (at 10 pps) is so low that the time-averaged activity level in the detector hall is barely above the natural cosmic radiation background.

The soft "tunnel shine" is only one part of the background problem. To reduce the beam size at the IP to small sizes it is necessary to make it larger at points upstream of the IP. The beam size reaches a maximum in the bore of the final quadrupole magnets which are located just outside the volume of the detector. If even a few particles per pulse strike the beam pipe inside these magnets then the detector will be inoperable, so it is necessary to collimate the beam to assure that this does not happen. Collimation of the beam at points in the final focus can be done but the FFS beamline is nearly straight and muons created in electromagnetic showers initiated by stopped beam particles have a high probability of reaching

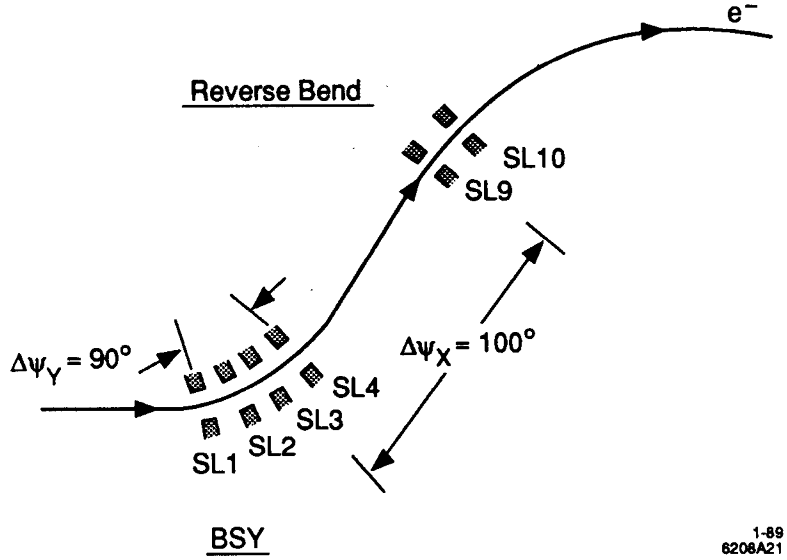

Fig. 32. Locations of collimators in the electron side of the BSY and ARC. There is an identical set of collimators for the e^+ beam.

the detector. Approximately one muon will be created (actually muons are pair-produced by the Bethe–Heitler process) with momentum above 1 GeV for every 10^4 electrons or positrons that are stopped, and the probability that such a muon will pass through the detector grows from a few percent to near unity as the location at which the muon is produced moves from the beginning of the FFS toward the detector. In practice it has been found impossible to operate the detector with primary collimation of the beam in the FFS.

The flux of muons passing through the detector has been controlled by moving the location of primary beam collimators upstream of the FFS to the beam switch yard (BSY) and ARCs, and by installation in the FFS of large toroidal magnets designed[19] to deflect locally-produced muons away from the detector and into the walls of the tunnel. The presently-installed collimation scheme for the machine is shown in Fig. 32. Primary collimation of the vertical phase space of the beam is done by slits SL1 and SL4 which are located in the BSY. These collimators are approximately 90° apart in betatron phase, so they affect an efficient removal of particles with large vertical betatron amplitudes. The horizontal collimation is not so ideal. There is insufficient horizontal phase advance in the BSY to allow for a complete collimation over this short distance of beamline. Slits SL3 in the BSY and SL9 in the ARC reverse bend are $\approx 90°$ apart, but cross-plane coupling in the ARC results in some repopulation of the vertical phase space before the horizontal collimation is complete. Furthermore, the horizontal dispersion is large in the BSY, so collimation of the horizontal betatron space is intertwined with collimation of the momentum tails of the beam (SL2 in the figure), and particles with appropriate correlation

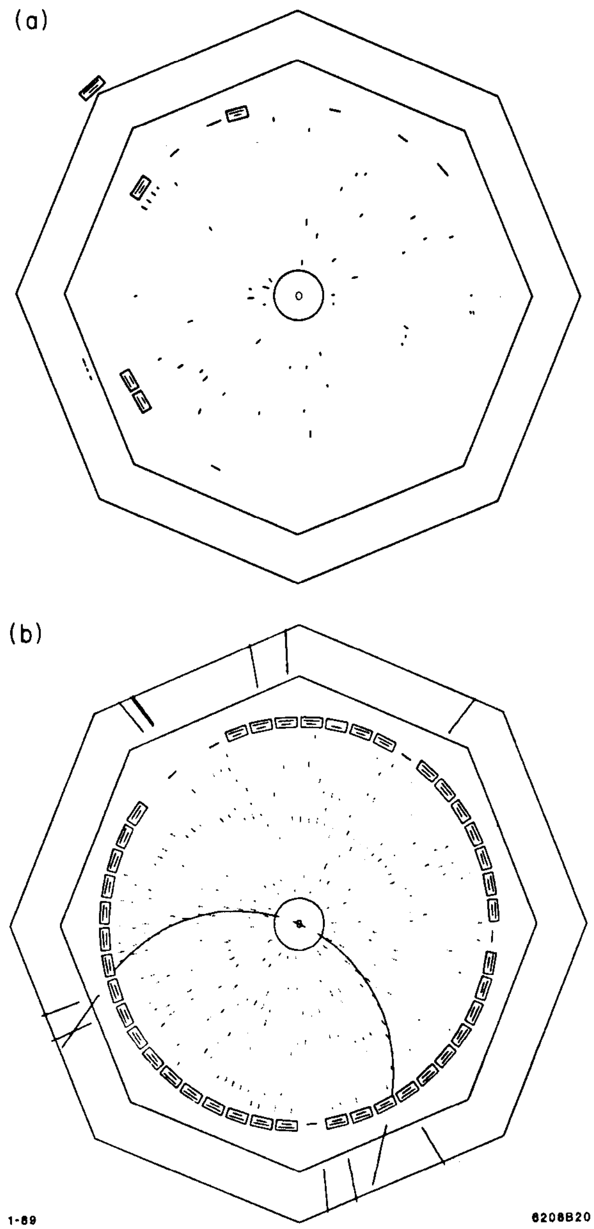

Fig. 33. Mark II triggers. (a) A randomly chosen beam crossing, and (b) a two-photon event of the type shown in Fig. 34. The invariant mass of the e^+e^- pair observed in the detector is 363 MeV, and the measured net transverse momentum of the pair is 4 MeV. The reconstructed origin of the pair is within 1 mm of the beamline in the transverse plane.

between energy and betatron phase can pass through the system. Slits located in the FFS are used to complete the collimation of the beam and to intercept secondary particles that are created by primary beam particles that strike the edges of the jaws of the BSY and ARC collimators and by the interactions of beam particles with the residual gas in the ARC beam pipe.

Fig. 34. Two-photon production of lepton pairs. The produced pair of leptons are characterized by low invariant masses and small momentum transfers.

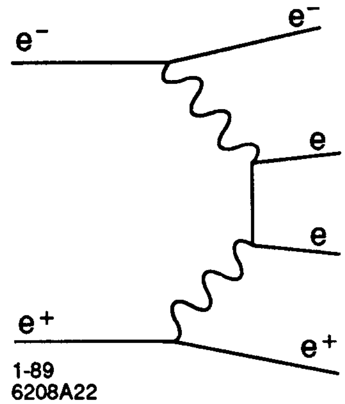

Experience has shown that this set of collimators is sufficient to allow efficient operation of the detector with beams of $\approx 10^{10}$ electrons and positrons with the FFS optics set to yield $\beta^* \approx 30$ mm. (See Fig. 24.) An additional set of collimators to be located in the last sector of the linac is being fabricated. These slits will provide complete and simultaneous collimation of both the electron and positron beams, and should be sufficient to allow operation at higher currents and smaller spot sizes.

Examples of triggers taken with the Mark II detector[20] are shown in Fig. 33. To produce Fig. 33(a), the detector was triggered on a randomly chosen crossing of a single pulse of $\approx 8 \times 10^9$ electrons. The detector operates quite efficiently in this environment. The two-particle charged trigger rate at 10 pps machine rate is less than 0.1 Hz and will create negligible dead time even at 120 pps. Figure 33(b) is an event that set the charged-particle trigger latch of the detector during a period of colliding beams. It is a two-photon event of the kind shown in Fig. 34. The two beam particles are scattered at small angles and pass down the beam pipe while the two soft particles are seen in the detector.

ACKNOWLEDGMENT

The SLC is the first of a new breed of facility that must be tamed if e^+e^- annihilation is to remain a tool for research in particle physics in the future. It is a joy to applaud the physicists, engineers, technicians and support crews who are pioneering this frontier of science.

REFERENCES

1. Physics at LEP, eds. J. Ellis and R. Peccei, CERN 86–02, 1986; *Proc. of the SLC Workshop on Experimental Use of the SLAC Linear Collider,* SLAC–REP–247, 1982.
2. These tests will require calculations of higher order electroweak corrections that depend on the presently unknown mass of the top quark and Higgs boson.
3. SLAC Linear Collider Conceptual Design Report, SLAC–REP–229, 1980.
4. J. Sheppard *et al.*, *Commissioning the SLC Injector*, contr. to the 1987 Particle Accelerator Conf., Washington, D.C., 1987.
5. A. Hutton *et al.*, IEEE Trans. Nucl. Sci. **32**, (5), 1059–1661, 1985.

6. J. Seeman and J. Sheppard, *Special SLC Linac Developments*, 1986 Linear Accelerator Conf., Stanford, CA, 1986;
   M. Allen *et al.*, *Performance of the Stanford Linear Collider Klystrons at SLAC*, contr. to the 1987 Particle Accelerator Conf., Washington, D.C., 1987.
7. K. Bane and T. Weiland, SLAC/AP–1, 1983.
8. J. Seeman, private communication.
9. R. Jobe *et al.*, SLAC–PUB–4703, contr. to the 1988 Linear Accelerator Conf. (LINAC 88), Williamsburg, VA, 1988.
10. V. Balakin, A. Novokhatsky and V. Smirnov, *Proc. of the 12th Int. Conf. on High Energy Accelerators*, Fermilab, 1983;
    K. Bane, SLAC/AP–69, 1988.
11. J. Seeman *et al.*, SLAC–PUB–4182, contr. to the 1987 Particle Accelerator Conf., Washington, D.C., 1987.
12. J. E. Clendenin *et al.*, SLAC–PUB–4704, contr. to the 1988 Linear Accelerator Conf. (LINAC 88), Williamsburg, VA, 1988.
13. T. Fiegut *et al.*, SLAC–PUB–4628, contr. to European Particle Accelerator Conf., Rome, 1988.
14. J. Murray, K. Brown and T. Fieguth, SLAC–PUB–4219, 1987, contr. to the 1987 Particle Accelerator Conf., Washington, D.C., 1987;
    R. Erickson, SLAC–PUB–4479, 1987. Lectures at the U.S. Summer School on High Energy Particle Accelerators, Batavia, Il, 1984.
15. C. Hawkes and P. Bambade, SLAC–PUB–4621 (also CALT–68–1495), 1988. Subm. to Nucl. Inst. and Meth. A.
16. P. Bambade, SLAC–PUB–4227, invited to the 1987 Particle Accelerator Conf., Washington, D.C., 1987.
17. W. Kozanecki, private communication.
18. G. Bowden *et al.*, SLAC–PUB–4744, 1989,, subm. to Nucl. Inst. and Methods A; R. Fulton *et al.*, SLAC–PUB–4605 (also LBL–25136 and UM–HE–88–10), 1988.
19. G. Feldman, private communication.
20. K. O'Shaughnessy *et al.*, SLAC–PUB–4558, 1988, subm. to Nucl. Inst. and Meth. A.